CHAPTER 4

LANTHANIDE SULFATE −4,4′−BIPYRIDINE FRAMEWORKS: SYNTHESIS, STRUCTURE, AND OPTICAL PROPERTIES

In spite of considerable progress achieved toward the understanding of photophysical behavior of the lanthanides, the subtle relationship that exists between the photophysical properties and structures suggests the need for further studies. It occurred to us that the lack of higher dimensional structures in sulfates and the need for larger coordination numbers for the lanthanide ions can be gainfully employed in preparing new 3−D lanthanide sulfate compounds. It has been shown that the use of 4,4′−bipyridine (4,4′−bipy) enhances dimensionality of the structures by acting as a rigid linker between the metal centers [1−7]. In addition, the use of 4,4′−bipy might assist in the luminescence behavior of the lanthanides through initial absorption and energy transfer. We used a combination of these during the preparation of a new family of lanthanide sulfate compounds. Our efforts were successful and we have isolated three new lanthanide sulfate compounds. The compounds $[C_{10}H_{10}N_2]_{0.5}[La(SO_4)_2].H_2O$ (**V**), $[C_{10}H_{10}N_2]_{0.5}[La(SO_4)_2(H_2O)_2]$ (**VIa**), $[C_{10}H_{10}N_2]_{0.5}[Pr(SO_4)_2(H_2O)_2]$ (**VIb**), $[C_{10}H_{10}N_2][Nd_2(SO_4)_4(H_2O)_2]$ (**VIIa**), $[C_{10}H_{10}N_2][Sm_2(SO_4)_4(H_2O)_2]$ (**VIIb**), and $[C_{10}H_{10}N_2][Eu_2(SO_4)_4(H_2O)_2]$ (**VIIc**) all have a 2−D layer structure formed by the connectivity between the rare earth ions and the sulfate units. The 4,4′−bipy ligand occupies the interlamellar spaces. In this chapter, we present the synthesis, structure, and photophysical properties of all the compounds.

4.1 Experimental section

4.1.1 Synthesis and initial characterization

The compounds reported in this chapter were prepared by the hydrothermal method. In a typical synthesis, for **V**, La_2O_3 (Merck, 99.5%; 0.2283 g, 0.70 mmol) was added to 10 cm^3 of deionized water. To this, 4,4′−bipy ($C_{10}H_8N_2$, 99% Fluka; 0.3283 g, 2.10 mmol) and concentrated sulfuric acid (H_2SO_4, 98% Merck; 0.3 cm^3) were added under continuous stirring. The mixture was homogenized for 30 min at room temperature. The final mixture was transferred, sealed in a 23 cm^3 PTFE lined autoclave, and heated at 200 °C for 24 h under autogenous pressure. The final product contained large quantities of colorless rod−shaped single crystals, which were filtered under a vacuum, washed with deionized water, and dried at ambient conditions (yield ~68% based on La). The other compounds were obtained employing similar conditions (Table 4.1). In the cases of Pr (**VIb**), Nd (**VIIa**), Sm (**VIIb**), and Eu (**VIIc**), the final products contain large quantities of light green (Pr), light purple (Nd), colorless (Sm), and colorless (Eu) rod−type single crystals, accordingly. In the case of compound **VIa**, the product was found to be a polycrystalline white powder. The product was later characterized by powder X−ray diffraction (PXRD) and then compared with the PXRD pattern of the related Pr compound (**VIb**). The PXRD pattern of **VIa** matched well with the simulated XRD pattern generated from the single crystal structure of Pr (**VIa**) compound. The microcrystalline phase **VIa** was indexed and the unit cell parameters were obtained from the PXRD patterns by the Le Bail method (Figure 4.1) [8].

Table 4.1 Synthesis conditions employed for the compounds.

Synthesis condition				
Mole ratio	**Temp (°C)**	**Time (h)**	**Yield (%)**	**Product**
(0.70) La_2O_3 + (2.10) 4,4′–bipy + (0.3) cm^3 of H_2SO_4 (conc.) + (556) H_2O	200	24	68	$[C_{10}H_{10}N_2]_{0.5}[La(SO_4)_2].H_2O$, (**V**)
(0.70) La_2O_3 + (2.10) 4,4′–bipy + (0.5) cm^3 of H_2SO_4 (conc.) + (556) H_2O	125	24	65	$[C_{10}H_{10}N_2]_{0.5}[La(SO_4)_2(H_2O)_2]$, (**VIa**)
(0.23) Pr_6O_{11} + (2.10) 4,4′–bipy + (0.5) cm^3 of H_2SO_4 (conc.) + (556) H_2O	125	24	63	$[C_{10}H_{10}N_2]_{0.5}[Pr(SO_4)_2(H_2O)_2]$, (**VIb**)
(0.70) Nd_2O_3 + (2.10) 4,4′–bipy + (0.5) cm^3 of H_2SO_4 (conc.) + (556) H_2O	125	24	72	$[C_{10}H_{10}N_2][Nd_2(SO_4)_4(H_2O)_2]$, (**VIIa**)
(0.70) Sm_2O_3 + (2.10) 4,4′–bipy + (0.5) cm^3 of H_2SO_4 (conc.) + (556) H_2O	125	24	68	$[C_{10}H_{10}N_2][Sm_2(SO_4)_4(H_2O)_2]$, (**VIIb**)
(0.70) Eu_2O_3 + (2.10) 4,4′–bipy + (0.5) cm^3 of H_2SO_4 (conc.) + (556) H_2O	125	24	70	$[C_{10}H_{10}N_2][Eu_2(SO_4)_4(H_2O)_2]$, (**VIIc**)

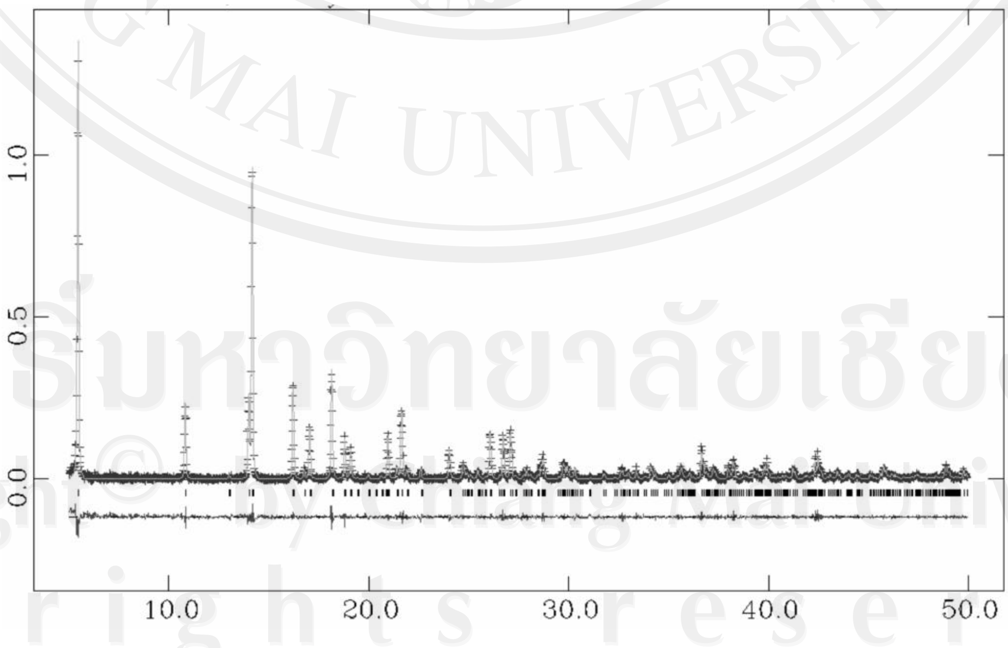

Figure 4.1 Le Bail fit of the compound **VIa**.

Initial characterizations were carried out by elemental analysis, PXRD, thermogravimetric analysis (TGA), and IR studies. PXRD patterns were recorded in the 2θ range 5–50° using Cu Kα radiation (Philips X'pert) (Figures 4.2–4.4). The IR spectra for the compounds were recorded as KBr pellets (Perkin–Elmer, SPECTRUM 1000). The IR spectroscopic studies exhibit typical peaks corresponding to the hydroxyl group, the amino groups, *etc.* (Figure 4.5). The main IR bands are (KBr): $\nu(H_2O)$ = 3230–3450 cm^{-1}, ν(N–H) = 3070–3110 cm^{-1}, ν(C–H) = 2670–2780 cm^{-1}, ν(C–H) = 1300–1500 cm^{-1}, $\nu_1(SO_4)$ = 950–1000 cm^{-1}, $\nu_3(SO_4)$ = 1100–1150 cm^{-1}, $\delta(SO_4)$ = 500–700 cm^{-1}. The IR spectrum can be useful for investigating the sulfate species. In general, the free sulfate ions exhibit two bands at 1105 and 615 cm^{-1}, which are assigned to the $\nu_3(T_2)$ stretching [ν_d(SO)] and $\nu_4(T_2)$ stretching [δ_d(OSO)] modes, respectively. The coordination of the sulfate group to the metal centers would lower the overall symmetry of the sulfate and lead to the splitting of the ν_3 and ν_4 modes. The IR spectra of the present compounds exhibits characteristic IR bands for the sulfate ions, SO_4^{-2}, with the IR–active region for the SO_4 tetrahedron located between 500 and 1150 cm^{-1}. In addition, we observed that the sulfate site symmetry is also lowered due to the many bridging coordination modes of the sulfate ions. The observed shoulders in the IR bands, thus, in the region 1025–1185 cm^{-1} may be attributed to the ν_3 modes and the shoulders in the region 554–670 cm^{-1} can be assigned to the ν_4 modes.

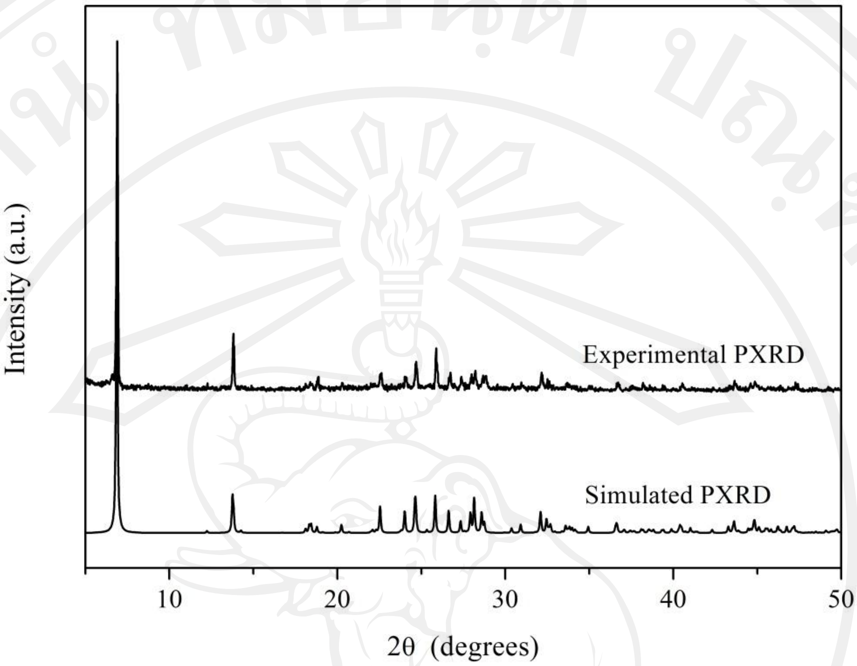

Figure 4.2 Powder X–ray diffraction pattern of compound **V**.

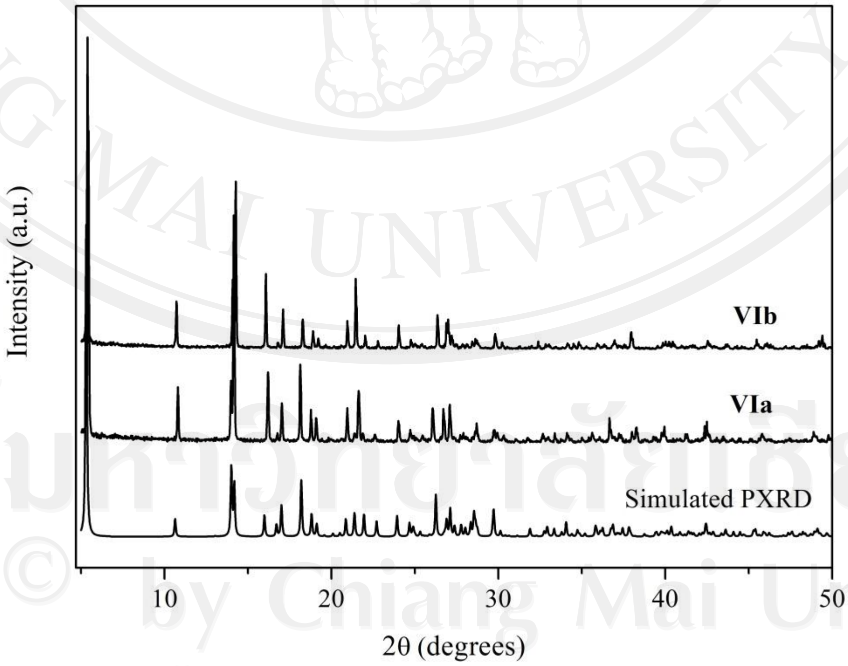

Figure 4.3 Powder X–ray diffraction patterns of compound **VIa** and **VIb.**

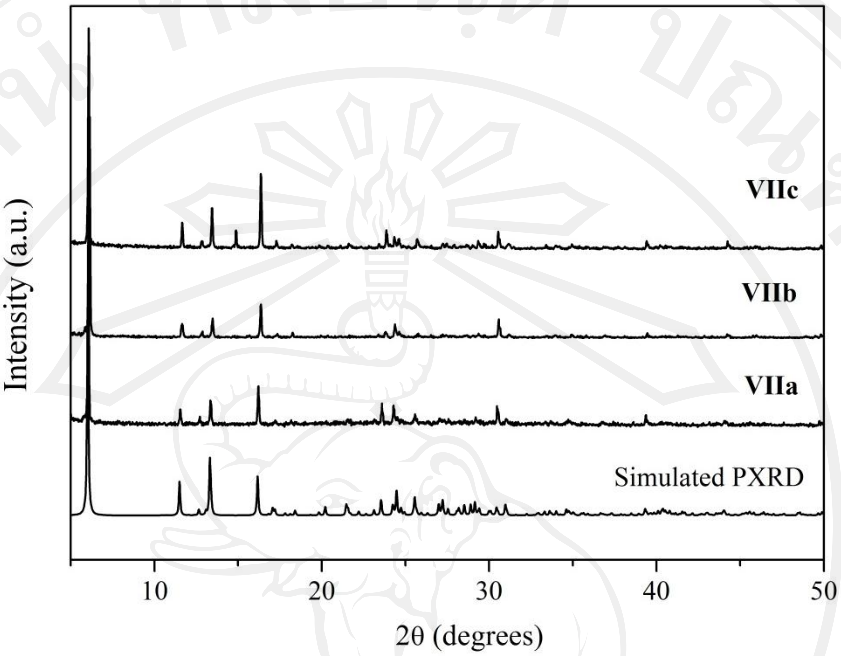

Figure 4.4 Powder X–ray diffraction patterns of compound **VIIa, VIIb** and **VIIc**.

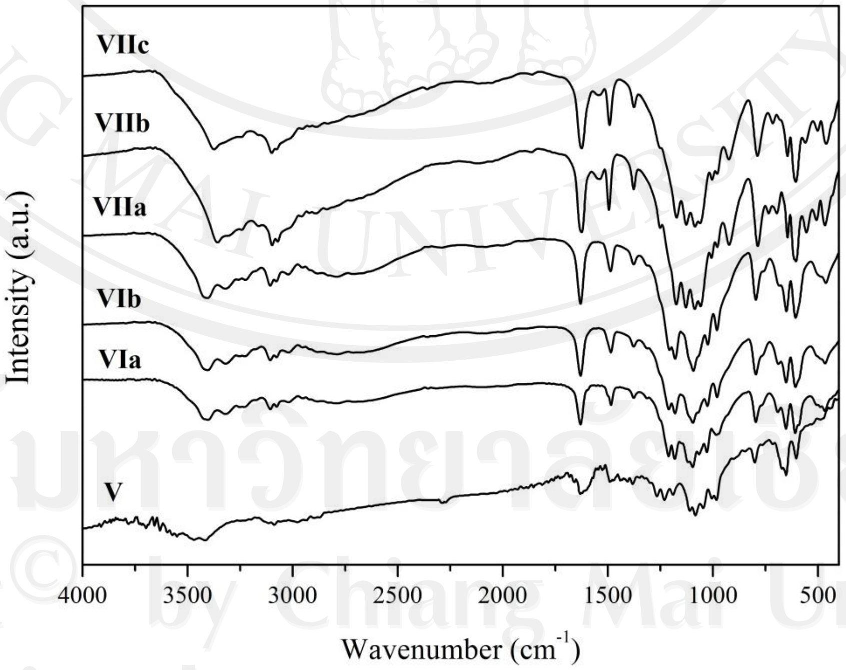

Figure 4.5 Room temperature IR spectra of the compounds.

4.1.2 Single crystal structure determination

A suitable single crystal of each compound was carefully selected under a polarizing microscope and glued to a thin glass fiber. The single crystal data were collected on a Bruker AXS smart Apex CCD diffractometer at 293(2) K. The X−ray generator was operated at 50 kV and 35 mA using Mo $K\alpha$ (λ = 0.71073 Å) radiation. Data were collected with ω scan width of 0.3°. A total of 606 frames were collected in three different settings of (0, 90, 180°) keeping the sample−to−detector distance fixed at 6.03 cm and the detector position (2θ) fixed at −25°. The data were reduced using SAINTPLUS [9], and an empirical absorption correction was applied using the SADABS program [10]. The structures were solved and refined using SHELXL97 [11] present in the WinGx suite of programs (Version 1.63.04a) [12]. All the hydrogen positions were initially located in the difference Fourier maps, and for the final refinement, the hydrogen atoms were placed in geometrically ideal positions and refined in the riding mode. Final refinement included atomic positions for all the atoms, anisotropic thermal parameters for all the non−hydrogen atoms, and isotropic thermal parameters for all the hydrogen atoms. Full−matrix least−squares refinement against $|F^2|$ was carried out using the WinGx package of programs [12]. Details of the structure solution and final refinements for the compounds are given in Table 4.2.

Table 4.2 Crystal data and structure refinement parameters for the compounds $[C_{10}H_{10}N_2]_{0.5}[La(SO_4)_2].H_2O$, (**V**) $[C_{10}H_{10}N_2]_{0.5}[Pr(SO_4)_2(H_2O)_2]$, (**VIb**), and $[C_{10}H_{10}N_2][Ln_2(SO_4)_4(H_2O)_2]_2$, (Ln= Nd (**VIIa**), Sm (**VIIb**) and Eu (**VIIc**).

Identification code	**V**	**VIb**	**VIIa**	**VIIb**	**VIIc**
Empirical formula	$C_5H_7NLaS_2O_9$	$C_5H_9NPrS_2O_{10}$	$C_{10}H_{14}N_2Nd_2S_4O_{18}$	$C_{10}H_{14}N_2Sm_2S_4O_{18}$	$C_{10}H_{14}N_2Eu_2S_4O_{18}$
Formula weight	426.13	448.16	866.95	875.14	878.36
Crystal system	triclinic	triclinic	triclinic	triclinic	triclinic
Space group	$P\bar{1}$	$P\bar{1}$	$P\bar{1}$	$P\bar{1}$	$P\bar{1}$
a/Å	5.6238(2)	5.0354(1)	8.0119(5)	7.9585(2)	7.9370(6)
b/Å	7.3489(3)	7.0079(1)	9.4075(6)	9.3752(3)	9.3612(7)
c/Å	12.9709(5)	16.6321(3)	14.9538(9)	14.9270(4)	14.9214(10)
α/°	90.821(2)	88.50	79.439(1)	79.327(2)	79.348(1)
β/°	96.912(2)	87.94	83.749(1)	83.927(2)	83.996(1)
γ/°	100.159(2)	75.47	73.988(1)	73.830(2)	73.777(1)
volume/Å^3	523.48(3)	567.67(2)	1062.99(11)	1049.44(5)	1044.52(13)
Z	2	2	2	2	2
T/K	293(2)	293(2)	293(2)	293(2)	293(2)
ρ_{calc} (g cm^{-3})	2.703	2.622	2.696	2.769	2.793
μ (mm^{-1})	4.522	4.711	5.320	6.036	6.448
θ range (°)	1.58–26.00	2.45–26.00	2.28–26.00	2.48–26.00	1.39–26.00
λ (Mo Kα) (Å)	0.71073	0.71073	0.71073	0.71073	0.71073
R_{int}	0.0262	0.0244	0.0252	0.0568	0.0416
reflection collected	7955	8568	11057	25572	10666
unique reflections	2007	2217	4159	4119	4082
no. of parameters	163	188	325	325	325
R, Rw (I>2σ(I))	0.0161, 0.0438	0.0160, 0.0428	0.0215, 0.0538	0.0420, 0.1141	0.0534, 0.1400
R, Rw (all data)	0.0163, 0.0439	0.0166, 0.0431	0.0249, 0.0551	0.0438, 0.1154	0.0542, 0.1412
Goodness of fit	1.141	1.130	1.079	1.042	1.085

4.1.3 Photoluminescence measurements of Eu^{III}/Tb^{III}−doped compounds

The Eu doped (4 mol% and 8 mol%) and Tb doped (4 mol% and 8 mol%) in place of La in **V** and Eu doped (4 mol% and 8 mol%) and Tb doped (4 and 8 mol%) in place of La in **VIa** were prepared using the same experimental procedure as that employed for **V** and **VIa**. The photoluminescence measurements were carried out on solid samples, using Perkin Elmer LS55 fluorescence spectrometer. The spectra were collected between 400 nm and 800 nm using a scan rate of 50 nmmin^{-1}.

4.2 Results and discussion

4.2.1 Structure of $[C_{10}H_{10}N_2]_{0.5}[La(SO_4)_2].H_2O$ (**V**)

The asymmetric unit of **V** consists of eighteen non−hydrogen atoms. It has one crystallographically independent La^{III} ion, two sulfate groups, half a molecule of protonated 4,4′−bipy molecule, and a lattice water molecule. The ORTEP diagram of extended asymmetric unit of compound **V** is shown in Figure 4.6. The half 4,4′−bipy unit is related to the other half through the C−C bond, which lies on the center of symmetry. The La^{III} ions are surrounded by nine sulfate oxygens forming a LaO_9 polyhedra, with a distorted tricapped trigonal prismatic coordination environment (Figure 4.7). The oxygen atoms O(3), O(5) and O(6) were found to be three coordinated, binding two La atoms and one S atom. The La−O bond distances are in the range of 2.473(2) – 2.623(2) Å and the selected bond distances are given in Table 4.3 and the refined atomic coordinates and equivalent isotropic displacement parameters are shown in Table 4.4. The structure of **V** consists of linkages between LaO_9 tricapped trigonal prisms and SO_4 tetrahedral units. The LaO_9 units are connected through three coordinated oxygen atoms [O(3), O(5), and O(6)] forming an infinite 2–D La–O–La network (Figure 4.8). The two sulfate tetrahedral units, $S(1)O_4$ and $S(2)O_4$, are connected to the La–O–La 2–D layers in such a way that they connects with four and three La atoms; 4.2210 and 3.2110 mode respectively, and each possess one terminal S=O bond [S(1)–O(7) and S(2)–S(8)] (Figure 4.9). The layers are arranged in a AAAA... fashion and are stabilized by the N–H···O and C–H···O interactions between the protonated bipyridinium cation and the framework oxygen (Figure 4.10) [13–14]. Details of hydrogen–bond interactions are given in Table 4.5.

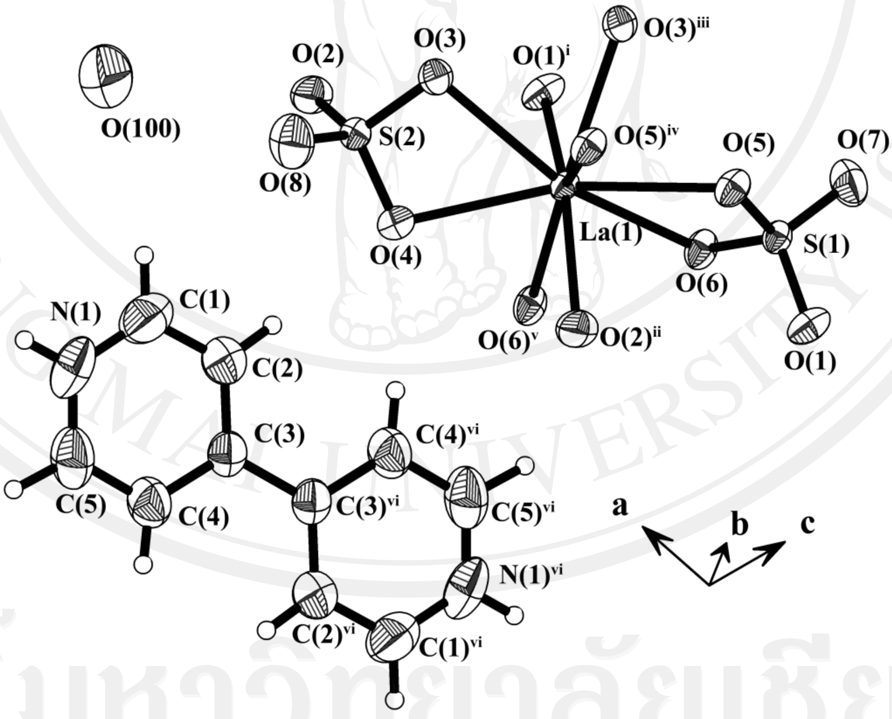

Figure 4.6 ORTEP diagram of extended asymmetric unit of compound **V**. Thermal ellipsoids are given at 80% probability. Symmetry codes: (i) [$x + 1$, y, z] (ii) [$x - 1$, y, z] (iii) [$-x + 1$, $-y + 1$, $-z + 2$] (iv) [$-x$, $-y + 1$, $-z + 2$] (v) [$-x$, $-y$, $-z + 2$] (vi) [$-x$, $-y$, $-z + 1$].

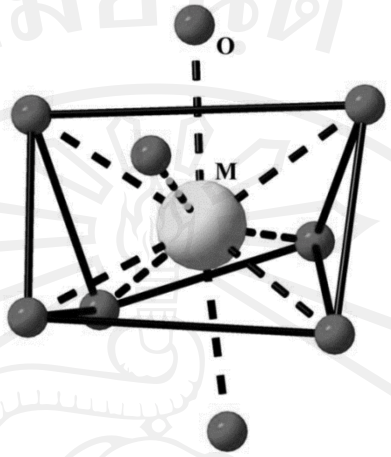

Figure 4.7 The distorted tricapped trigonal prismatic geometry of the central metal ion of compound **V**.

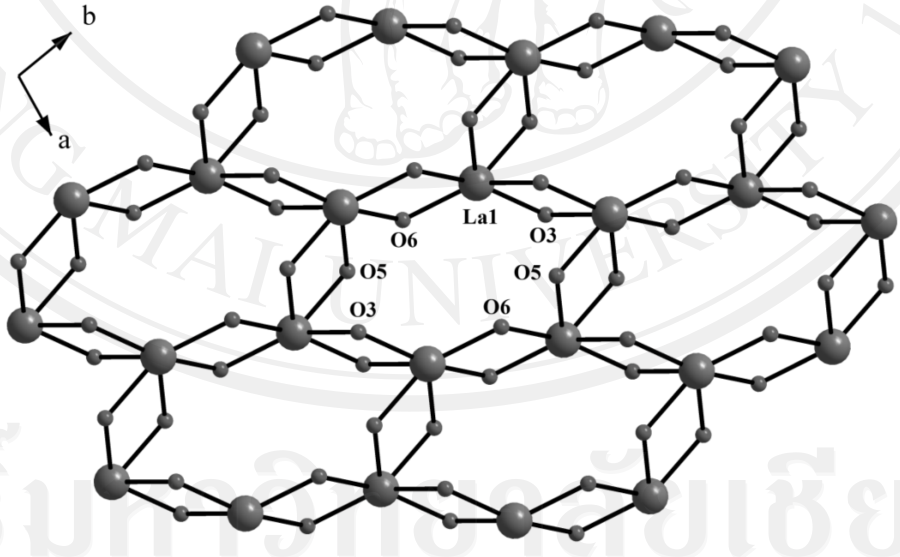

Figure 4.8 View of the 2−D infinite La−O−La layer in **V**. Only the lanthanide ion connectivity is shown.

Table 4.3 Selected bond distances in the compound **V**.

Bond distances (Å) ^{a}			
La(1)–O(1)^{i}	2.473(2)	S(1)–O(1)	1.462(2)
La(1)–O(2)^{ii}	2.474(2)	S(1)–O(5)	1.502(2)
La(1)–O(3)^{iii}	2.555(2)	S(1)–O(6)	1.5032(2)
La(1)–O(4)	2.555(1)	S(1)–O(7)	1.440(2)
La(1)–O(5)^{iv}	2.575(2)	S(2)–O(8)	1.448(2)
La(1)–O(5)	2.589(2)	S(2)–O(2)	1.472(2)
La(1)–O(6)^{v}	2.610(2)	S(2)–O(3)	1.507(2)
La(1)–O(3)	2.613(2)	S(2)–O(4)	1.487(2)
La(1)–O(6)	2.623(2)		

^{a} Symmetry codes: (i) [$x + 1, y, z$] (ii) [$x - 1, y, z$] (iii) [$-x + 1, -y + 1, -z + 2$] (iv) [$-x, -y + 1, -z + 2$] (v) [$-x, -y, -z + 2$].

Table 4.4 Atomic coordinates ($\times 10^4$) and equivalent isotropic displacement parameters ($Å^2 \times 10^3$) for **V**.

	x	***y***	***z***	***U(eq)***
La(1)	1907(2)	2813(2)	9629(1)	10(7)
O(1)	−4839(3)	1616(3)	10724(2)	18(4)
O(2)	8140(4)	2569(3)	8396(2)	20(4)
O(3)	5795(3)	4758(3)	9007(2)	16(4)
O(4)	3755(4)	2149(3)	7989(2)	19(4)
O(5)	−1129(3)	3897(2)	10749(2)	14(4)
O(6)	−879(3)	740(2)	10801(2)	15(4)
O(7)	−2027(4)	2256(3)	12297(2)	23(5)
O(8)	6377(4)	4547(3)	71781(2)	28(5)
S(1)	−2293(1)	2117(9)	11178(5)	11(1)
S(2)	6068(1)	3516(9)	8110(5)	12(1)
N(1)	4878(5)	2093(4)	3760(2)	32(7)
C(1)	4893(7)	2461(5)	4775(3)	36(8)
C(2)	2992(6)	1647(5)	5276(3)	31(7)
C(3)	1052(5)	452(4)	4736(2)	21(6)
C(4)	1115(6)	103(5)	3677(2)	28(7)
C(5)	3051(7)	944(5)	3204(3)	33(8)
O(100)	10678(6)	4861(5)	6107(3)	73(1)

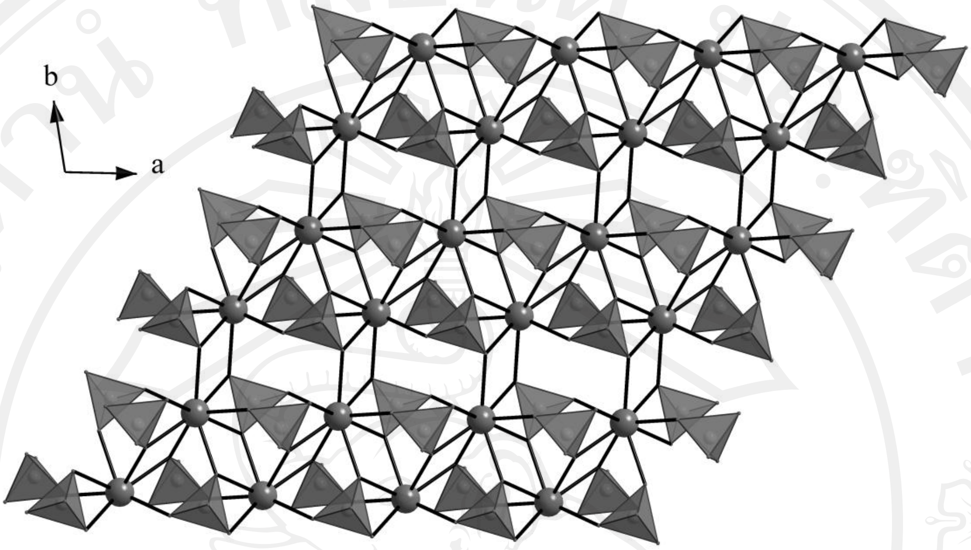

Figure 4.9 View of the 2−D lanthanide sulfate layer in the *ab* plane in **V**.

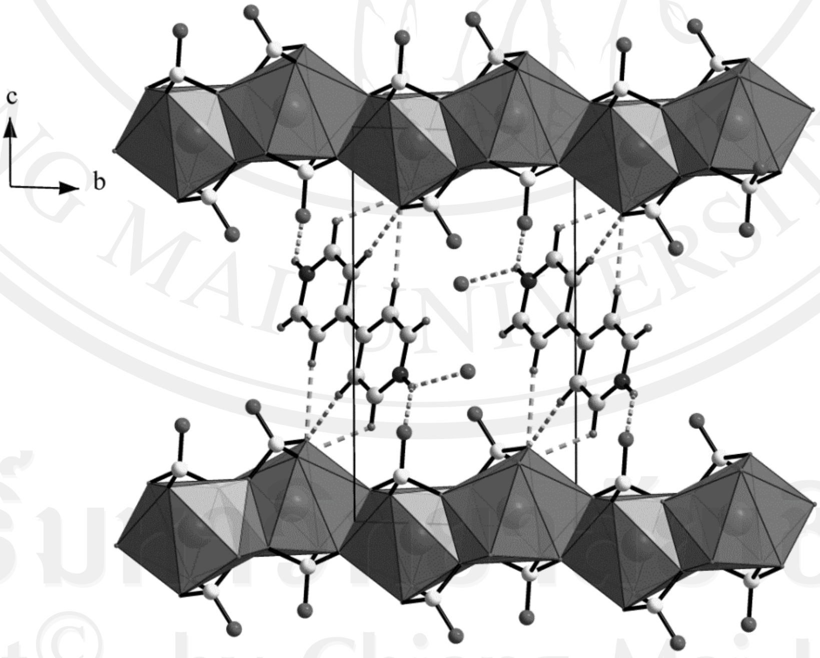

Figure 4.10 The arrangement of layers in the *bc* plane (**V**). Note that the 4,4′−bipy molecules occupy interlamellar spaces along with the water molecules.

Table 4.5 Details of the hydrogen bonds interactions in **V**. A hydrogen bond donor is signified as D–H, where D is the donor atom. The hydrogen bond acceptor atom is labeled A.

D–H ··· A[a]	D–H, (Å)	H ··· A, (Å)	D ··· A, (Å)	D–H ··· A, (°)
N(1)–H(1A) ··· O(100)[vii]	0.86	2.37	3.033(5)	134
N(1)–H(1A) ··· O(7)[viii]	0.86	1.98	2.716(4)	143
C(2)–H(2) ··· O(4)	0.93	2.58	3.499(4)	168
C(4)–H(4) ··· O(4)[vi]	0.93	2.52	3.433(4)	165

[a] Symmetry codes: (vii) [–*x* + 2, –*y* + 1, –*z* + 1] (viii) [*x* + 1, *y*, *z* – 1].

4.2.2 Structure of $[C_{10}H_{10}N_2]_{0.5}[Pr(SO_4)_2(H_2O)_2]$ (VIb)

The asymmetric unit of **VIb** consists of nineteen non–hydrogen atoms. It has one crystallographically independent Pr^{III} atoms, two sulfate units, half a molecule of protonated 4,4′–bipy molecule, and two coordinated water molecules (Figure 4.11). The Pr^{III} ions are coordinated by seven sulfate oxygen and two aqua oxygen (O(3) and O(7)) forming a PrO_9 polyhedra with a distorted tricapped trigonal prism arrangement (Figure 4.12). The half 4,4′–bipy molecule is related to the other half *via* the C–C bond, which lies on the center of symmetry. The Pr–O bond distances are in the range of 2.402(2)–2.820(2) Å (av. 2.539 Å). The selected bond distances are detailed in Table 4.6. The refined atomic coordinates and equivalent isotropic displacement parameters are shown in Table 4.7.

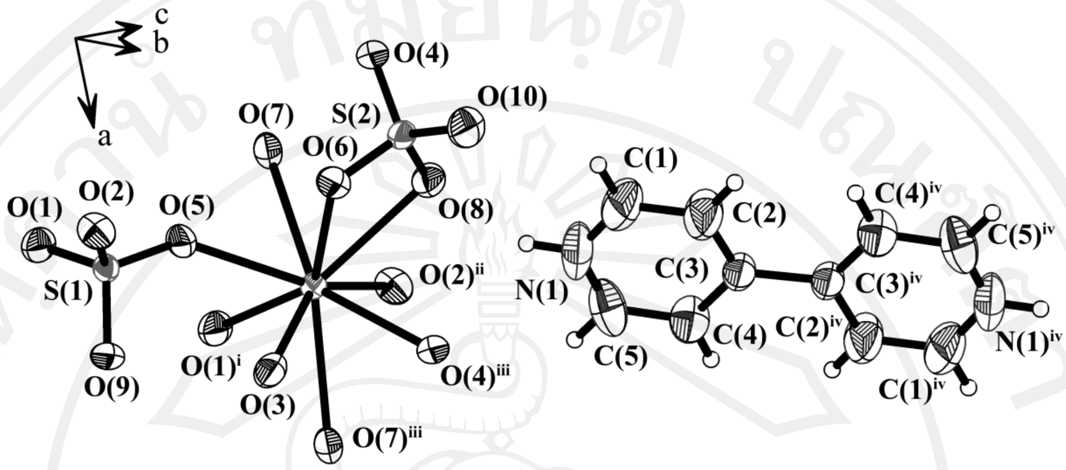

Figure 4.11 ORTEP diagram of extended asymmetric unit of compound **VIb**. Thermal ellipsoids are given at 80% probability. Symmetry codes: (i) [–*x* + 1, –*y*, –*z*] (ii) [*x*, *y* + 1, *z*] (iii) [*x* + 1, *y*, *z*] (iv) [–*x* + 1, –*y* + 2, –*z* + 1].

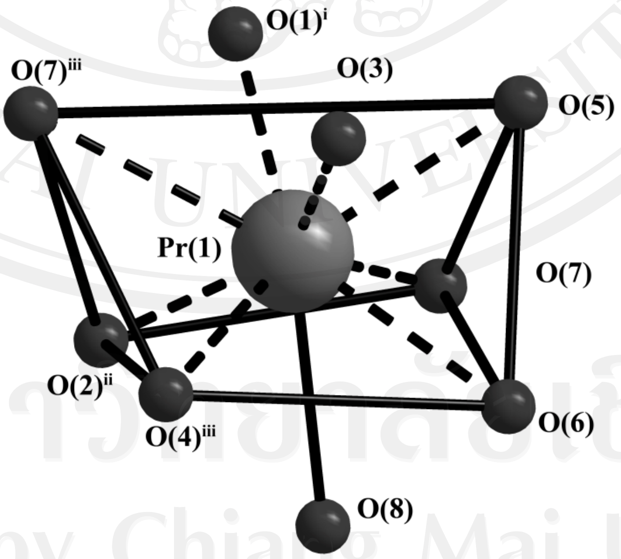

Figure 4.12 The distorted tricapped trigonal prismatic geometry of the central metal ion of compound **VIb.**

Table 4.6 Selected bond distances in the compound **VIb**.

Bond distance (Å) ^{a}			
Pr(1)–O(1)^{i}	2.402(2)	S(1)–O(1)	1.470(2)
Pr(1)–O(2)^{ii}	2.434(2)	S(1)–O(2)	1.477(2)
Pr(1)–O(3)	2.469(2)	S(1)–O(5)	1.465(2)
Pr(1)–O(4)^{iii}	2.480(2)	S(1)–O(9)	1.482(2)
Pr(1)–O(5)	2.504(2)	S(2)–O(6)	1.495(2)
Pr(1)–O(6)	2.527(2)	S(2)–O(8)	1.491(2)
Pr(1)–O(7)	2.602(2)	S(2)–O(4)	1.483(2)
Pr(1)–O(8)	2.615(2)	S(2)–O(10)	1.451(2)
Pr(1)–O(7)^{iii}	2.820(2)		

^{a} Symmetry codes: (i) [–*x* + 1, –*y*, –*z*] (ii) [*x*, *y* + 1, *z*] (iii) [*x* + 1, *y*, *z*].

Table 4.7 Atomic coordinates (×10^4) and equivalent isotropic displacement parameters (Å^2 × 10^3) for **VIb**.

	x	***y***	***z***	***U(eq)***
Pr(1)	5174(3)	2555(2)	1525(9)	11(7)
O(1)	4020(5)	–2549(3)	–94(1)	20(5)
O(2)	4402(5)	–3926(3)	1248(14)	19(5)
O(3)	8765(5)	–452(3)	1862(15)	22(5)
O(4)	–2276(5)	3243(3)	2687(14)	20(5)
O(5)	3995(5)	–470(3)	1035(14)	18(5)
O(6)	2394(5)	1214(3)	2591(14)	17(5)
O(7)	209(4)	3311(3)	993(13)	16(4)
O(8)	1641(5)	4679(3)	2543(14)	18(5)
O(9)	8168(4)	–2823(3)	631(14)	17(5)
O(10)	707(5)	3095(4)	3799(14)	25(5)
S(1)	5138(15)	–2430(10)	702(4)	11(5)
S(2)	583(15)	3061(11)	2930(5)	14(2)
N(1)	4132(8)	6655(5)	3588(2)	36(8)
C(1)	2869(10)	6684(7)	4305(3)	45(1)
C(2)	3226(10)	7970(7)	4875(3)	40(1)
C(3)	4851(7)	9266(5)	4700(2)	20(7)
C(4)	6159(8)	9150(5)	3947(2)	27(8)
C(5)	5764(9)	7816(6)	3399(2)	33(9)

The structure of **VIb** consists of a linkage between PrO_9 and SO_4 units forming a 2–D structure. The Pr atoms are connected through a μ_2 oxygen atom forming 1–D Pr–O–Pr infinite chains (Figure 4.13). The sulfate tetrahedral $S(1)O_4$ (3.1110 mode) connects the Pr–O–Pr chains forming the 2–D structure, which is anionic (Figure 4.14). The other sulfate tetrahedral $S(2)O_4$ (2.1110 mode) connects only to the Pr centers and is not employed in extending the dimensionality of the structure. This arrangement appears to satisfy the coordination requirement of the central Pr atoms only. Another view to understand the structure is to consider the connectivity between PrO_9 and $S(2)O_4$ polyhedral units, which forms a 1–D edge–shared ladder–like structure (Figure 4.15). The ladder units are connected with the Pr–O–Pr linkages giving rise to the 2–D layers. The layers are arranged in a AAAA… fashion and the interlamellar space is occupied by the protonated bipyridinium cataions (Figure 4.16). Both strong and weak hydrogen bond interactions are observed between the bipyridinium cation and the anion framework, which are detailed in Table 4.8.

Table 4.8 Details of the hydrogen bonds interactions in **VIb**. A hydrogen bond donor is signified as D–H, where D is the donor atom. The hydrogen bond acceptor atom is labeled A.

D–H ··· A ^{a}	D–H, (Å)	H ··· A, (Å)	D ··· A, (Å)	D–H ··· A, (°)
N(1)–H(1) ··· O(4)^{iii}	0.86	2.47	3.010(4)	121
N(1)–H(1) ··· O(8)	0.86	1.97	2.768(4)	155
C(1)–H(1) ··· O(10)	0.93	2.38	3.126(6)	137
C(2)–H(2) ··· O(10)^{v}	0.93	2.28	3.112(6)	148
C(5)–H(5) ··· O(3)^{ii}	0.93	2.48	3.282(5)	145

^{a} Symmetry codes: (ii) [x, y + 1, z] (iii) [x + 1, y, z] (v) [–x, –y + 1, –z + 1].

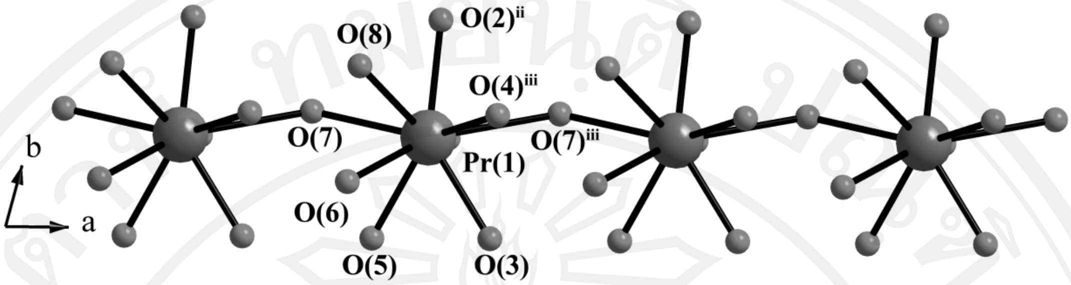

Figure 4.13 The 1–D infinite Pr–O–Pr chains observed in $[C_{10}H_{10}N_2]_{0.5}[Pr(SO_4)_2(H_2O)_2]$, **VIb**.

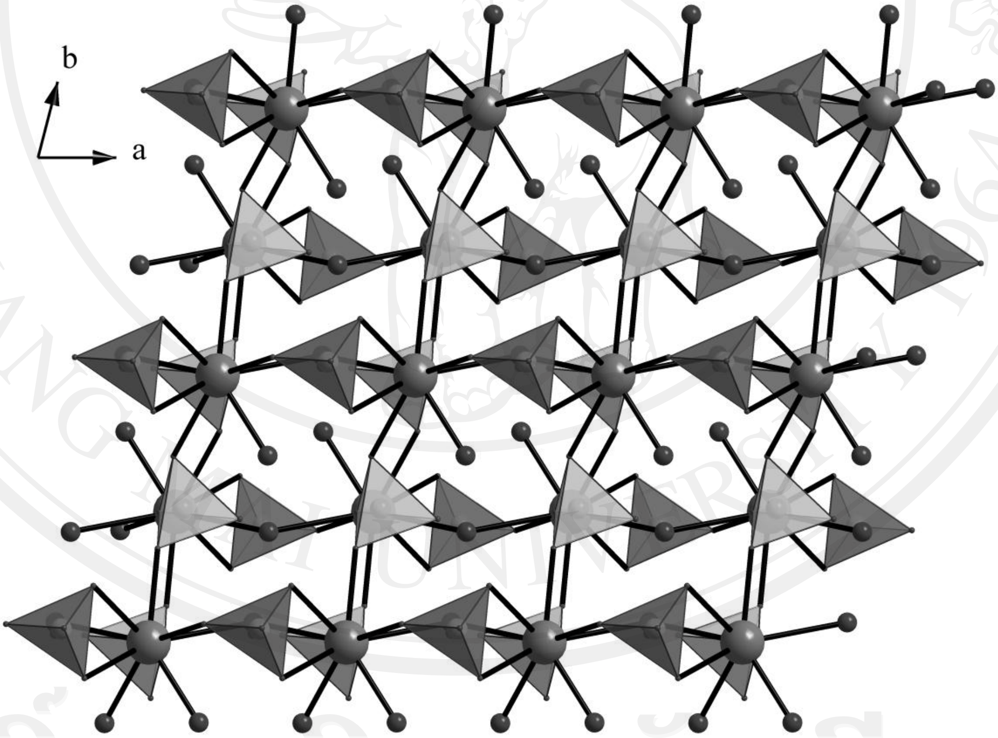

Figure 4.14 View of the 2–D praseodymium sulfate layer in the *ab* plane. Note that the bound water molecules project out of the plane of the layers. $S(1)O_4$ and $S(2)O_4$ are represented by light grey and dark grey polyhedral, respectively.

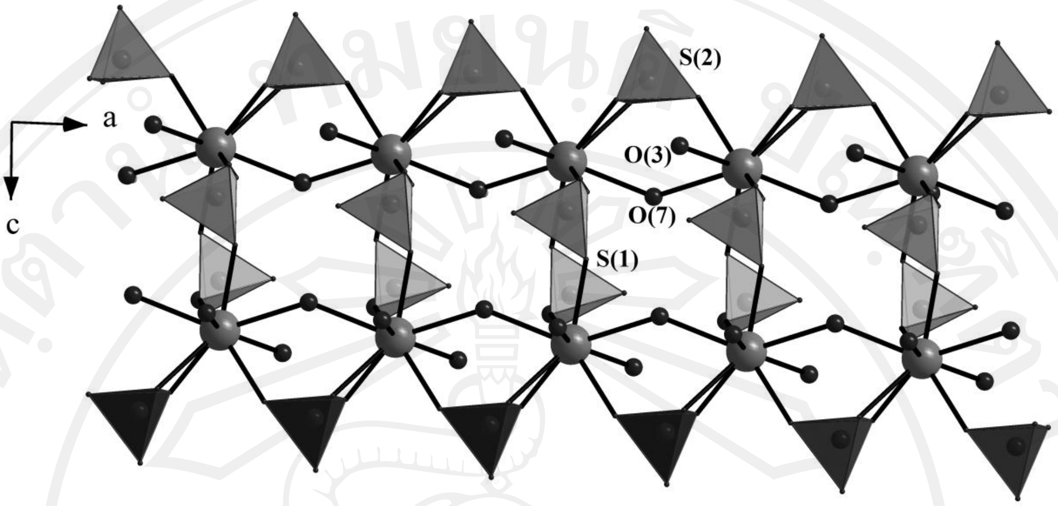

Figure 4.15 1−D edge−shared ladder−like chain, running along *b* axis in compound **VIb**.

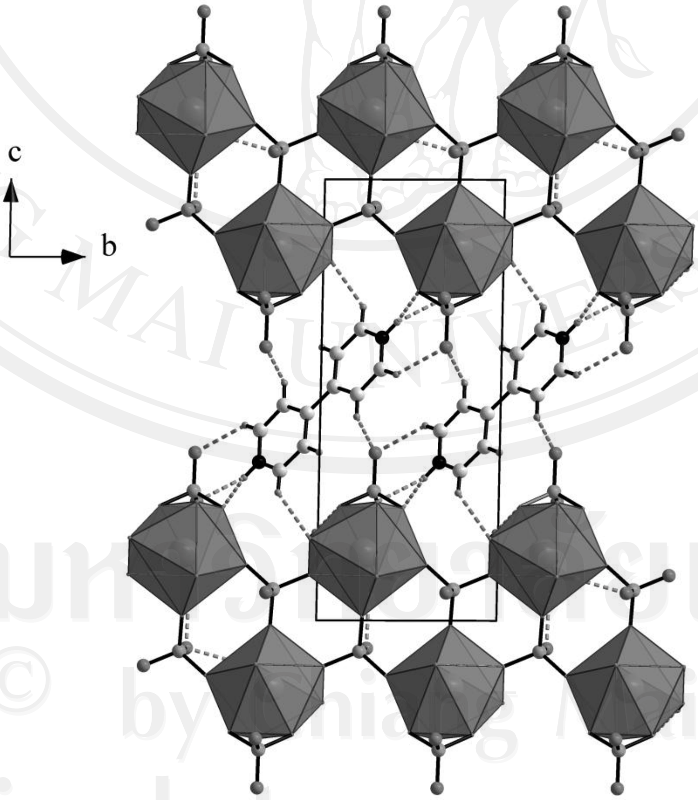

Figure 4.16 3−D arrangement of the layers in the *bc* plane.

4.2.3 Structure of $[C_{10}H_{10}N_2][Ln_2(SO_4)_4(H_2O)_2]$, Ln = Nd^{III} (VIIa), Sm^{III} (VIIb), and Eu^{III} (VIIc)

The asymmetric unit of $[C_{10}H_{10}N_2][Ln_2(SO_4)_4(H_2O)_2]$, Ln = Nd^{III} (**VIIa**), Sm^{III} (**VIIb**) and Eu^{III} (**VIIc**) consists of thirty–six non–hydrogen atoms. It has two crystallographically independent Ln^{III} ion ($Ln(1)^{III}$ and $Ln(2)^{III}$), four sulfate groups, one protonated 4,4′–bipy molecule, and two coordinated water molecules (Figure 4.17). The $Ln(1)^{III}$ ions are surrounded by eight sulfate oxygen and one aqua oxygen (O(2)) to form a $Ln(1)O_9$ polyhedra, which has a distorted tricapped trigonal prismatic coordination environment. In the case of $Ln(2)^{III}$ ions, seven sulfate oxygen and one aqua oxygen (O(12)) surround the central metal atom forming a $Ln(2)O_8$ polyhedra, with a distorted square antiprism coordination geometry (Figure 4.18). The oxygen atoms, O(4) and O(8), are three coordinated connecting two metal centers and a sulfate unit.

The Ln–O bond distances are in the following ranges Nd: 2.340(2)–2.731(2) Å (av. 2.490 Å); Sm: 2.306(4)–2.734(4) Å (av. 2.462 Å) and Eu: 2.292(4)–2.733(4) Å (av. 2.450 Å). The selected bond distances are given in Table 4.9 and the refined atomic coordinates and equivalent isotropic displacement parameters are shown in Table 4.10.

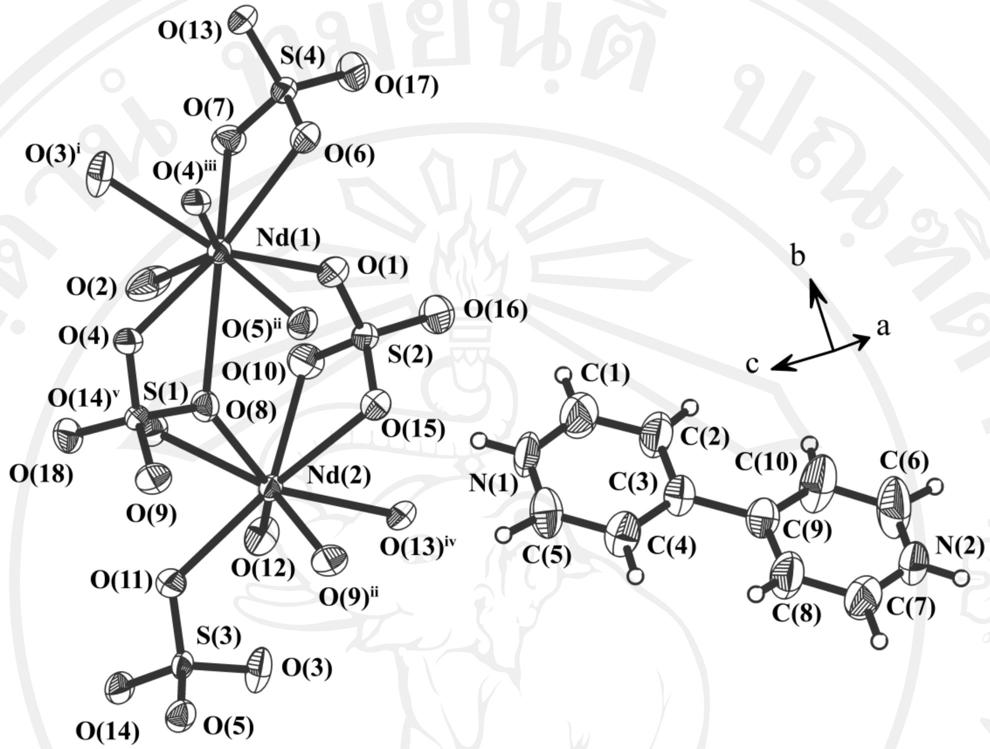

Figure 4.17 ORTEP diagram of extended asymmetric unit of compound **VIIa**. Thermal ellipsoids are given at 80% probability. Symmetry codes: (i) [*x*, *y* + 1, *z*] (ii) [–*x* + 1, –*y*, –*z* + 1] (iii) [–*x* + 1, –*y* + 1, –*z* + 1] (iv) [*x*, *y* – 1, *z*] (v) [–*x*, –*y*, –*z* + 1].

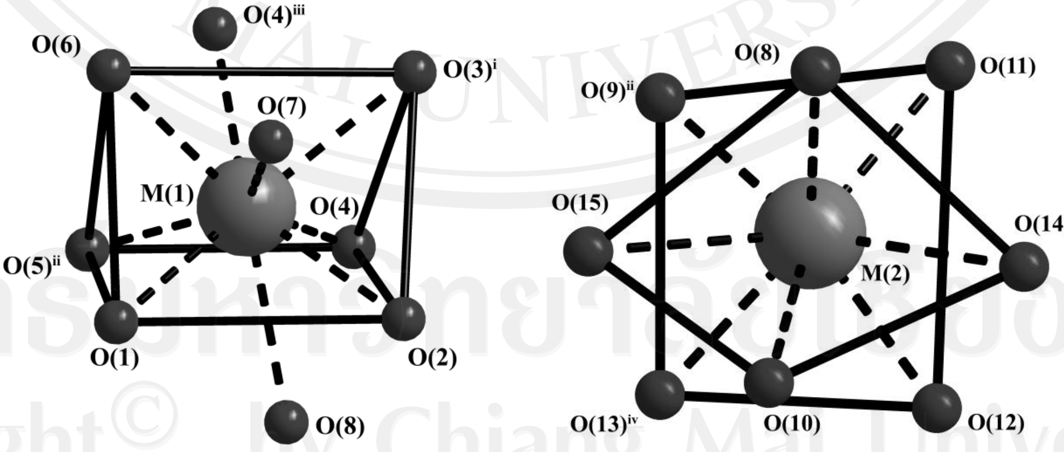

Figure 4.18 The distorted tricapped trigonal prismatic and distorted square antiprismatic geometry of the central metal ions of compound **VIIa**.

Table 4.9 Selected bond distances and angles in the compound **VIIa**.

Bond distance (Å) [a]			
Nd(1)–O(1)	2.378(3)	S(2)–O(1)	1.478(3)
Nd(1)–O(2)	2.429(3)	S(3)–O(3)	1.479(3)
Nd(1)–O(3)^{i}	2.460(3)	S(1)–O(4)	1.509(2)
Nd(2)–O(9)^{ii}	2.340(2)	S(3)–O(5)	1.466(3)
Nd(2)–O(10)	2.423(3)	S(4)–O(6)	1.508(3)
Nd(2)–O(11)	2.470(3)	S(4)–O(7)	1.494(3)
Nd(1)–O(4)	2.471(2)	S(1)–O(8)	1.489(2)
Nd(1)–O(5)^{ii}	2.482(2)	S(1)–O(9)	1.458(3)
Nd(1)–O(6)	2.490(3)	S(2)–O(10)	1.485(3)
Nd(2)–O(12)	2.473(3)	S(3)–O(11)	1.482(3)
Nd(2)–O(13)^{iv}	2.489(2)	S(4)–O(13)	1.477(3)
Nd(2)–O(14)^{v}	2.509(2)	S(3)–O(14)	1.479(3)
Nd(1)–O(7)	2.526(2)	S(2)–O(15)	1.489(3)
Nd(1)–O(4)^{iii}	2.603(2)	S(2)–O(16)	1.443(3)
Nd(1)–O(8)	2.731(2)	S(4)–O(17)	1.442(3)
Nd(2)–O(8)	2.517(2)	S(1)–O(18)	1.443(3)
Nd(2)–O(15)	2.548(3)		

[a] Symmetry codes: (i) [*x*, *y* + 1, *z*] (ii) [–*x* + 1, –*y*, –*z* + 1] (iii) [–*x* + 1, –*y* + 1, –*z* + 1] (iv) [*x*, *y* – 1, *z*] (v) [–*x*, –*y*, –*z* + 1].

Table 4.10 Atomic coordinates (×10^4) and equivalent isotropic displacement parameters (Å^2 × 10^3) for **VIIa**.

	x	***y***	***z***	***U(eq)***
Nd(1)	3924(2)	5095(2)	3800(12)	11(6)
Nd(2)	2616(2)	493(2)	3713(12)	11(6)
O(1)	4153(4)	4093(3)	2430(18)	21(6)
O(2)	914(3)	4979(3)	3945(2)	26(7)
O(3)	2281(3)	–2783(3)	4557(2)	21(6)
O(4)	3945(3)	3936(3)	5423(2)	13(5)

Table 4.10 Atomic coordinates (×10^4) and equivalent isotropic displacement parameters (Å^2 × 10^3) for **VIIa** (continued).

	x	***y***	***z***	***U(eq)***
O(5)	3199(3)	–3230(3)	6095(2)	17(5)
O(6)	5282(3)	6683(3)	2582(2)	16(5)
O(7)	2212(3)	7140(3)	2651(2)	17(6)
O(8)	3413(3)	2343(3)	4497(2)	15(5)
O(9)	4736(3)	1243(3)	5925(2)	18(6)
O(10)	2064(3)	2656(3)	2519(2)	20(6)
O(11)	2075(3)	–698(3)	5294(2)	17(6)
O(12)	151(3)	–264(3)	3258(2)	21(6)
O(13)	3456(3)	9250(3)	2338(2)	18(6)
O(14)	165(3)	–2289(3)	5832(2)	17(5)
O(15)	5017(3)	1386(3)	2701(2)	17(5)
O(16)	4154(4)	2740(3)	1213(2)	27(7)
O(17)	3799(4)	7681(3)	1189(2)	26(7)
O(18)	1744(3)	2590(3)	5942(2)	18(6)
S(1)	3431(1)	2496(9)	5469(6)	10(2)
S(2)	3856(1)	2734(1)	2183(6)	14(2)
S(3)	1942(1)	–2265(9)	5451(6)	11(2)
S(4)	3675(1)	7716(1)	2154(6)	13(2)
N(1)	7025(5)	–422(4)	1514(2)	27(8)
N(2)	12808(5)	–4712(4)	–1390(2)	27(8)
C(1)	6944(6)	17(5)	617(3)	37(1)
C(2)	8092(6)	–793(5)	27(3)	36(1)
C(3)	9357(5)	–2079(4)	376(3)	21(8)
C(4)	9369(5)	–2480(5)	1314(3)	24(9)
C(5)	8178(5)	–1634(5)	1871(3)	27(9)
C(6)	11614(6)	–3539(6)	–1744(3)	40(1)
C(7)	13010(6)	–5074(5)	–498(3)	34(1)
C(8)	11923(6)	–4214(5)	86(3)	34(1)
C(9)	10606(5)	–2985(4)	–252(3)	21(8)
C(10)	10492(6)	–2648(6)	–1179(3)	36(1)

In the structure of **VIIa**, the LnO_9 and LnO_8 polyhedral units are linked with the sulfate tetrahedra giving rise to a 2−D anionic layer structure. The $Ln(1)O_9$ units are linked through the three−connected oxygen atom, O(8), with $Ln(2)O_8$ units forming a four−membered cluster (Figure 4.19). The sulfate tetrahedral units; $S(1)O_4$, $S(2)O_4$, $S(3)O_4$ and $S(4)O_4$ bridge the four−membered clusters with the 4.2210, 2.1110, 4.1111 and 2.1110 mode, respectively, giving rise to the 2−D layer arrangement with an overall anionic layer of the formula, $[Ln_2(SO_4)_4(H_2O)_2]^{2-}$ (Figure 4.20). The charge is balanced by the presence of the protonated bipyridinium cations, which occupies the interlamellar spaces as in Figure 4.21. A number of hydrogen bond interactions have been observed which appears to be strong [18] and detailed in Table 4.11.

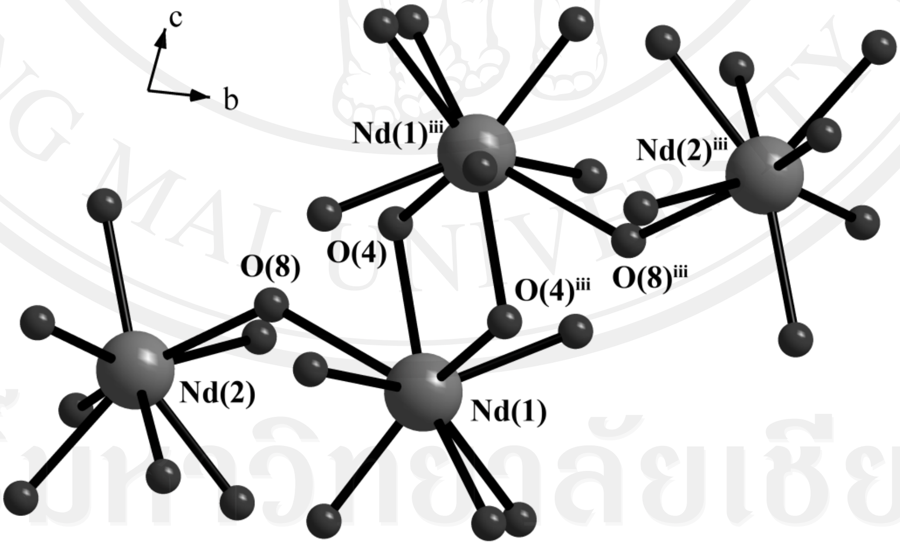

Figure 4.19 View of the tetrameric unit found in $[C_{10}H_{10}N_2][Nd_2(SO_4)_4(H_2O)_2]_2$, **VIIa**.

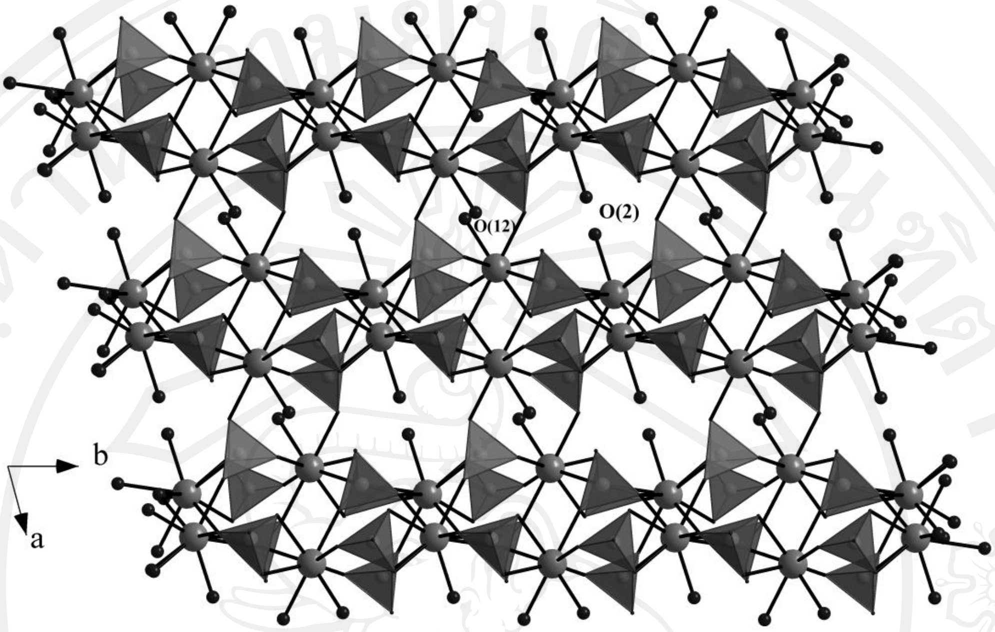

Figure 4.20 The 2−D layer in the *ab* plane.

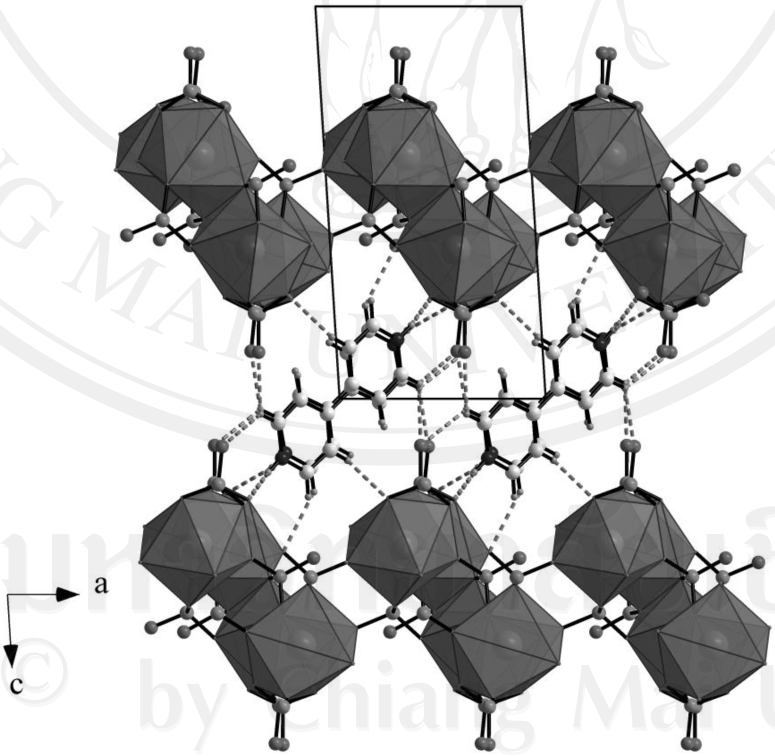

Figure 4.21 3−D arrangement of the layers in **VIIa**.

Table 4.11 Details of the hydrogen bonds interactions in **VIIa**. A hydrogen bond donor is signified as D–H, where D is the donor atom. The hydrogen bond acceptor atom is labeled A.

D–H ··· A [a]	D–H, (Å)	H ··· A, (Å)	D ··· A, (Å)	D–H ··· A, (°)
N(1)–H(1) ··· O(15)	0.86	1.91	2.758(4)	170
N(2)–H(2) ··· O(1)^{vi}	0.86	2.48	2.883(5)	109
N(2)–H(2) ··· O(6)^{vi}	0.86	1.98	2.830(4)	171
C(1)–H(1A) ··· O(16)	0.93	2.43	3.098(5)	129
C(1)–H(1A) ··· O(17)^{vii}	0.93	2.50	3.136(5)	125
C(4)–H(4) ··· O(7)^{viii}	0.93	2.58	3.098(5)	115
C(5)–H(5) ··· O(18)^{ix}	0.93	2.30	3.232(5)	179
C(6)–H(6) ··· O(5)^{x}	0.93	2.53	3.332(5)	145
C(7)–H(7) ··· O(16)^{viii}	0.93	2.35	3.027(5)	129
C(7)–H(7) ··· O(17)^{vi}	0.93	2.59	3.242(6)	128
C(10)–H(10) ··· O(10)^{xi}	0.93	2.60	3.020(5)	108

[a] Symmetry codes: (vi) [–*x* + 2, –*y*, –*z*] (vii) [–*x* + 1, –*y* + 1, –*z*] (viii) [*x* + 1, *y* – 1, *z*] (ix) [–*x* +1, –*y*, –*z* + 1] (x) [*x* + 1, *y*, *z* – 1] (xi) [–*x* + 1, –*y*, –*z*].

4.2.4 Structural comparison

The three structures (**V**, **VIb**, and **VIIa**) identified in the present chapter have some common features: (i) the lanthanide ions have predominantly a tricapped trigonal prismatic coordination; (ii) the lanthanide ions are connected through the three–coordinated oxygen atoms forming 2–D La–O–La layers in **V**, a 1–D chain in **VIb** and a four–member cluster in **VIIa**. In addition, the sulfate connectivity in these structures also exhibit subtle differences. The sulfate groups participate in bonding between two lanthanide centers in **V**, while half the sulfate units in **VIa** and **VIIa** appear to satisfy the coordination requirement of the lanthanide centers only. With the Harris notation, the coordination modes of sulfate units in **V** can be defined as 4.2210

(S(1)) and 3.2110 (S(2)), in **VIb** are 3.1110 (S(1)) and 2.110 (S(2)), in **VIIa** are 4.2210 (S(1)), 2.1110 (S(2) and S(4)) and 4.1111 (S(3)). The larger coordination (8 and 9) requirement of the lanthanide ions could be responsible for this, which also resulted in having coordinated aqua ligands in the structures of **VIa** and **VIIa**. Exclusive use of ligands for coordination requirements is not new, and examples of such roles for the participating ligands have been observed earlier in framework compounds [15−16]. The presence of 4,4′−bipy as a cation in the structure is also important and noteworthy. In many framework compounds, the 4,4′−bipy generally binds with the metal centers extending dimensionality [17−19], but here it performs the role of a template molecule. When the lanthanide connectivity alone is considered in these structures, we observed a honeycomb arrangement in the cases of **V** and **VIIa**, whereas a square−grid results for **VIb** (Figure 4.22). The formations of such networks in lanthanide containing compounds are rare.

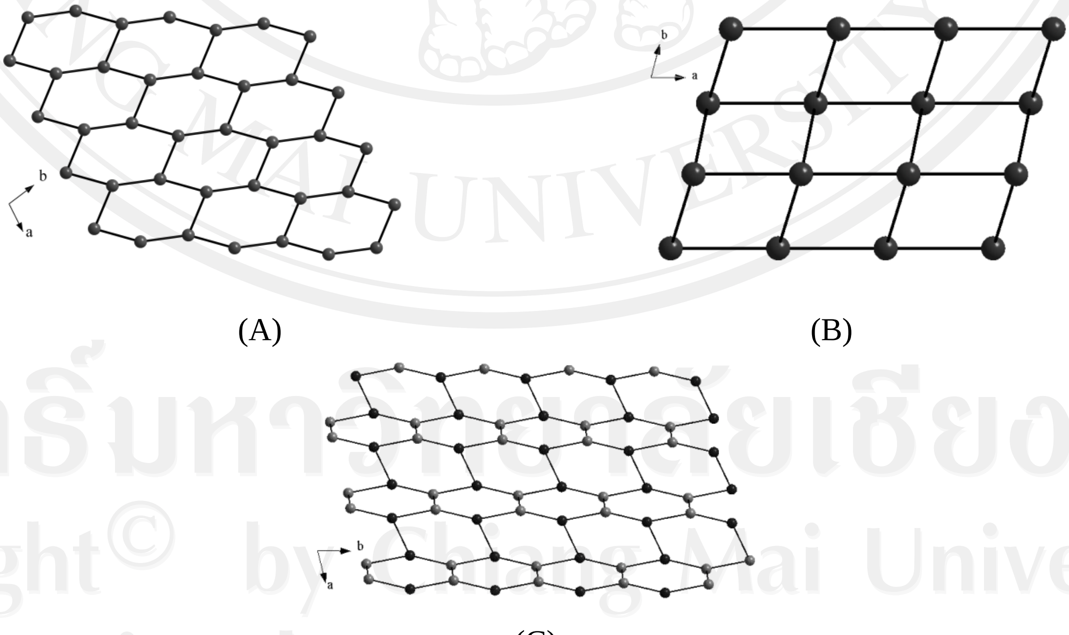

(A) (B)

(C)

Figure 4.22 The lanthanide ion connectivity in the structures: (A) the honeycomb layer in **V**; (B) the square−grid layer in **VIb**; (C) the honeycomb layer in **VIIa**.

4.2.5 Thermogravimetric studies

TGA on all the compounds has been carried out in flowing air (flow rate = 20 cm^{3}min^{-1}) in the temperature range 30−850 °C (heating rate = 5 °C min^{-1}). All the compounds exhibit comparable thermal behavior as shown in Figure 4.23−4.25. For compound **V**, two step weight losses were observed. The first weight loss of 3.7% observed in the range 150−250 °C corresponds to the loss of water molecules (4.2%). The second sharper weight loss of 44.9% in the range 480−520 °C corresponds to the loss of the 4,4′−bipy and some sulfate (calc. 46.5%). In the case of **VIa** and **VIb** we observed an almost identical behavior in terms of the weight losses though the total weight loss was different. The first weight loss of 7.8% in the range 140−190 °C corresponds to the loss of water molecules (calc. 8% for **VIa** and **VIb**). The second weight loss 31.2% for **VIa** and 44.2% for **VIb** in the range 410−500 °C corresponds to the losses of the 4,4′−bipy and sulfate (calc 44.4%for **VIa**: 45.6% for **VIb**). In the case of compounds **V** and **VIa**, the calcined product was found to be crystalline and corresponds to the compound $La_2O_2SO_4$ (JCPDS: 85−1535). In the case of **VIb**, the final calcined product was found to be $Pr_2O_2SO_4$ (JCPDS: 29−1073). The TGA behavior of compounds **VIIa**, **VIIb**, and **VIIc** are also similar, exhibiting a two−step weight loss. For **VIIa**, the first weight loss of 3.7% in the range 180−250 °C, corresponds to the loss of the coordinated water molecules (calc. 4.4%). The second weight loss of 25.3% in the range 470−500 °C is followed by another loss. The total weight loss of 55% corresponds to the loss of the 4,4′−bipy along with some sulfate. The calcined product was found to be crystalline and corresponds to the phase $Nd_2O_2SO_4$ (JCPDS: 48−1829). Similarly for **VIIb** and **VIIc**, we observed the formation of $Sm_2O_2SO_4$ (JCPDS: 41−0681) and $Eu_2O_2SO_4$ (JCPDS: 48−1211) phases after the TGA studies.

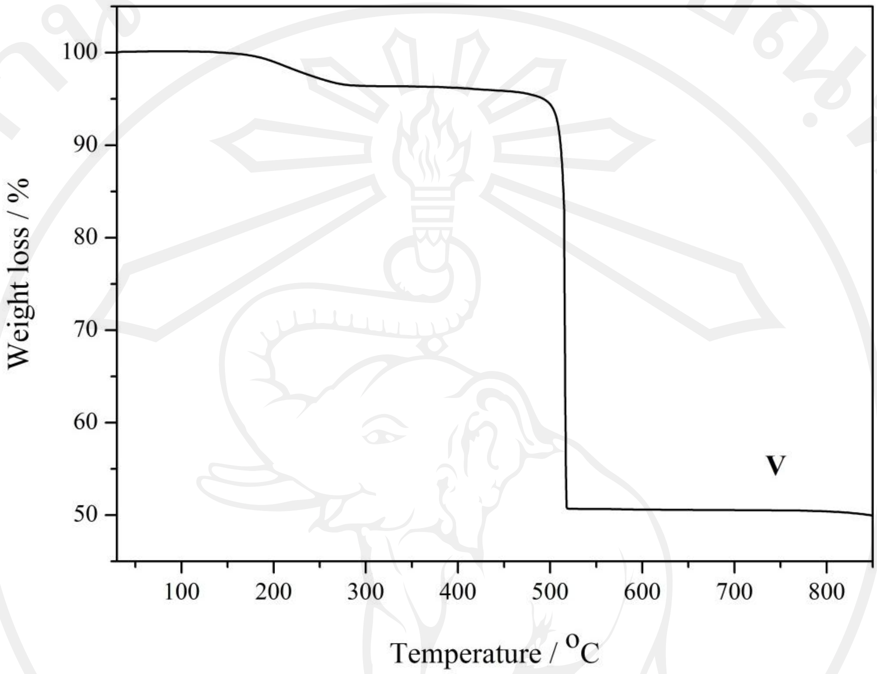

Figure 4.23 Thermogravimetric analysis (TGA) of compound **V**.

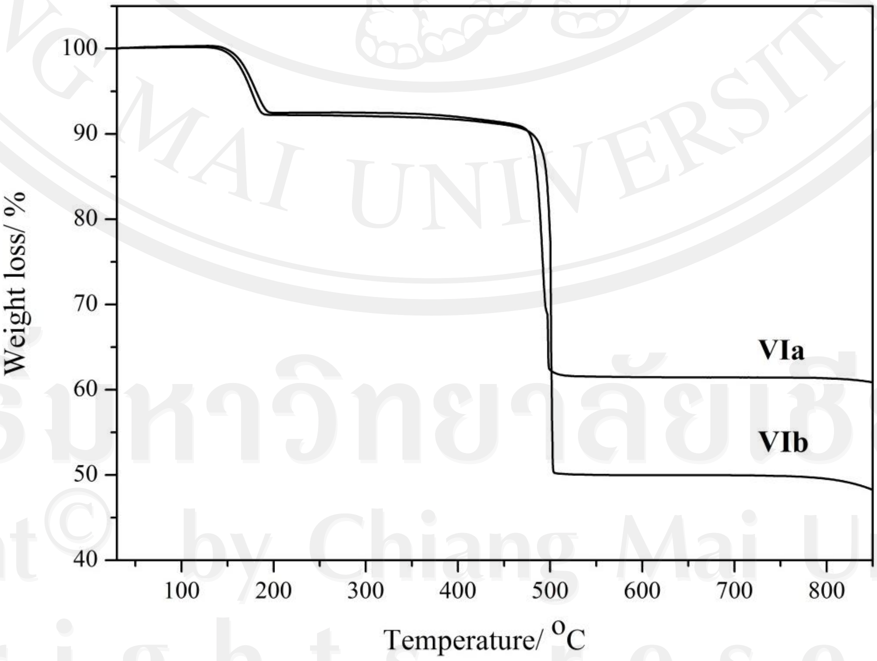

Figure 4.24 Thermogravimetric analysis (TGA) of compounds **VIa** and **VIb**.

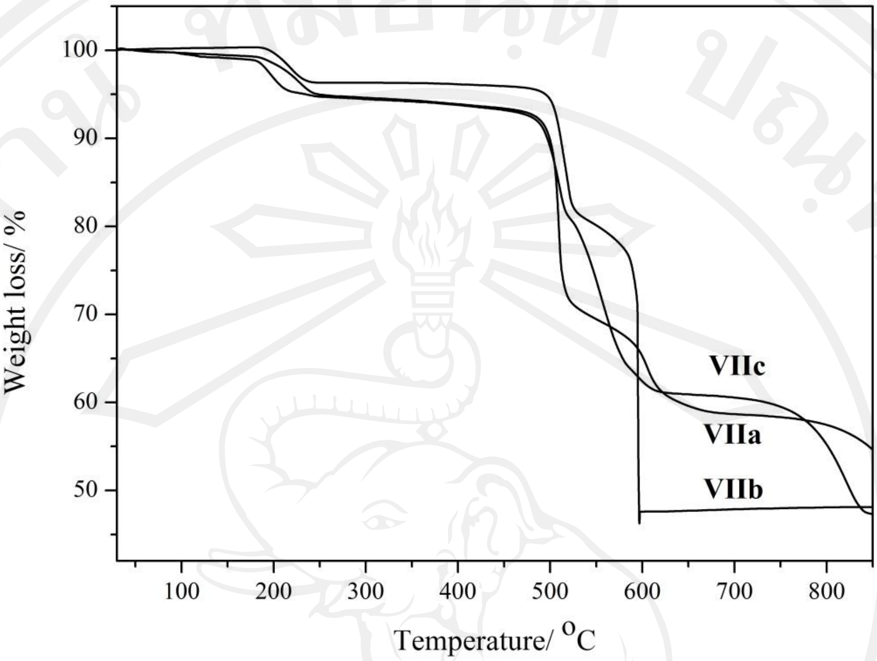

Figure 4.25 Thermogravimetric analysis (TGA) of compounds **VIIa**, **VIIb** and **VIIb**.

4.2.6 Luminescence studies

All the compounds exhibited one strong absorption band centered around 450 nm, which corresponds to the ligand to metal charge transfer (LMCT), when excited using a wavelength of 310 nm. To probe and to appreciate the LMCT effect further, we have prepared two sets of compounds by doping a small concentration of Eu^{III} and Tb^{III} (4% and 8%) in place of La^{III} (compounds **V** and **VIa**). The results of the photoluminescence studies were shown in Figures 4.26 and 4.27. The doped samples exhibited sharp characteristics peaks, in addition to the LMCT peak at 450 nm. We also observed a pink color for Eu^{III} doped samples and a green color for the Tb^{III} doped samples when observed under the UV illumination. When excited using a wavelength of 310 nm, we observed the characteristic $^{5}D_{0} \rightarrow {}^{7}F_{J}$ (J = 1, 2) emission lines for Eu^{III} and $^5D_4 \rightarrow {}^7F_J$ (J = 3, 4, 5, 6) emission lines for Tb^{III}, respectively. It may be noted the intensity of the characteristic lanthanide emission due to Eu^{III} and Tb^{III} is not strong, suggesting that the energy transfer process in the present compounds are quite poor. This situation is in contrast to the behavior observed in many of the lanthanide benzene carboxylate frameworks, where intense lanthanide emissions have been observed [20–21]. Even though the intensity of the emission in the present compounds is not strong; we sought to investigate the lifetime of the excited states in the doped compounds.

4.2.7 Lifetime studies

The luminescence lifetimes of the excited states of the 4 mol% doped samples of **V** and **VIa** were investigated. The $^5D_0 \rightarrow {}^7F_1$ band for the Eu^{III} samples **V** (4% Eu) and **VIa** (4% Eu) and the $^5D_4 \rightarrow {}^7F_6$ emission band for the Tb^{III} samples **V** (4% Tb) and **VIa** (4% Tb) were monitored for the lifetime studies employing 310 nm excitation at room temperature. The experimental luminescent decay curve was fitted to a single exponential decay function as,

$$I = I_0 \exp(-t/\tau)$$

where I and I_0 stand for the luminescent intensities at time t = t and t = 0, respectively, and τ is defined as the luminescent lifetime. The fit of the curve for a single exponential decay suggests a lifetime value of 0.38 ms for **V** (4% Eu) (Figure 4.28). The lifetime values for the other samples are given in Table 4.12 and Figure 4.29. The values of the lifetime observed in the present compounds are comparable to the values generally known for the pure Eu^{III} and Tb^{III} compounds reported in the literature [22].

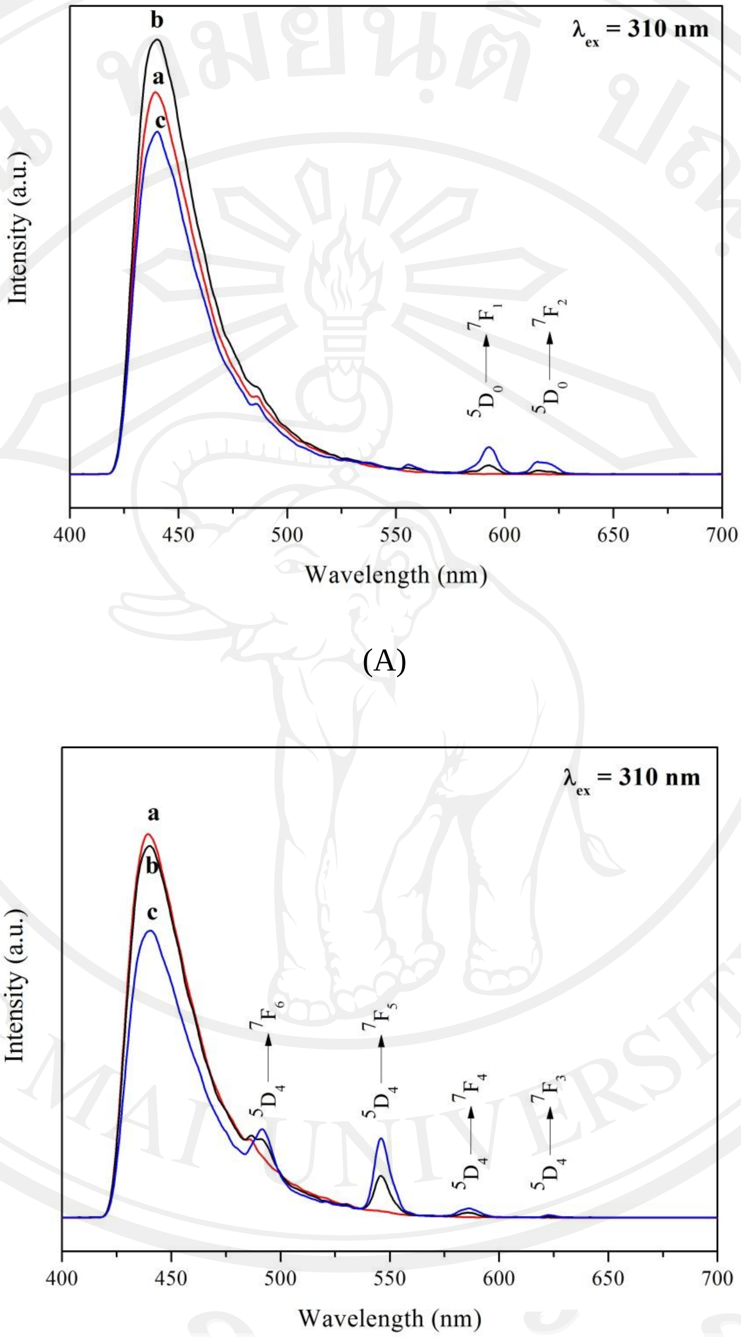

(A)

(B)

Figure 4.26 Room temperature photoluminescence spectra of compound **V** and the corresponding Eu^{III} and Tb^{III} doped samples. (A) (a) Compound **V**, (b) 4 mol% and (c) 8 mol% Eu^{III} doped samples. (B) (a) Compound **V**, (b) 4 mol% and (c) 8 mol% Tb^{III} doped samples.

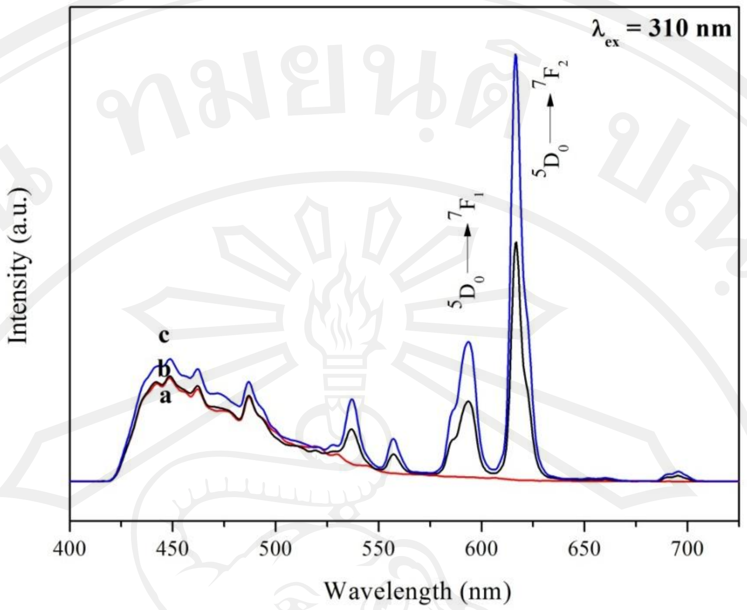

(A)

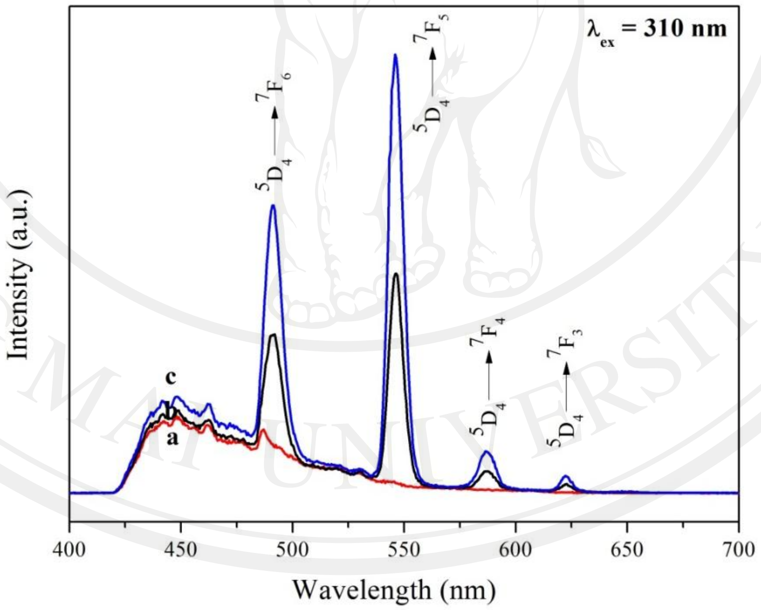

(B)

Figure 4.27 Room temperature photoluminescence spectra of compound **VIa** and the corresponding Eu^{III} and Tb^{III} doped samples. (A) (a) Compound **VIa**, (b) 4 mol% and (c) 8 mol% Eu^{III} doped samples. (B) (a) Compound **VIa**, (b) 4 mol% and (c) 8 mol% Tb^{III} doped samples.

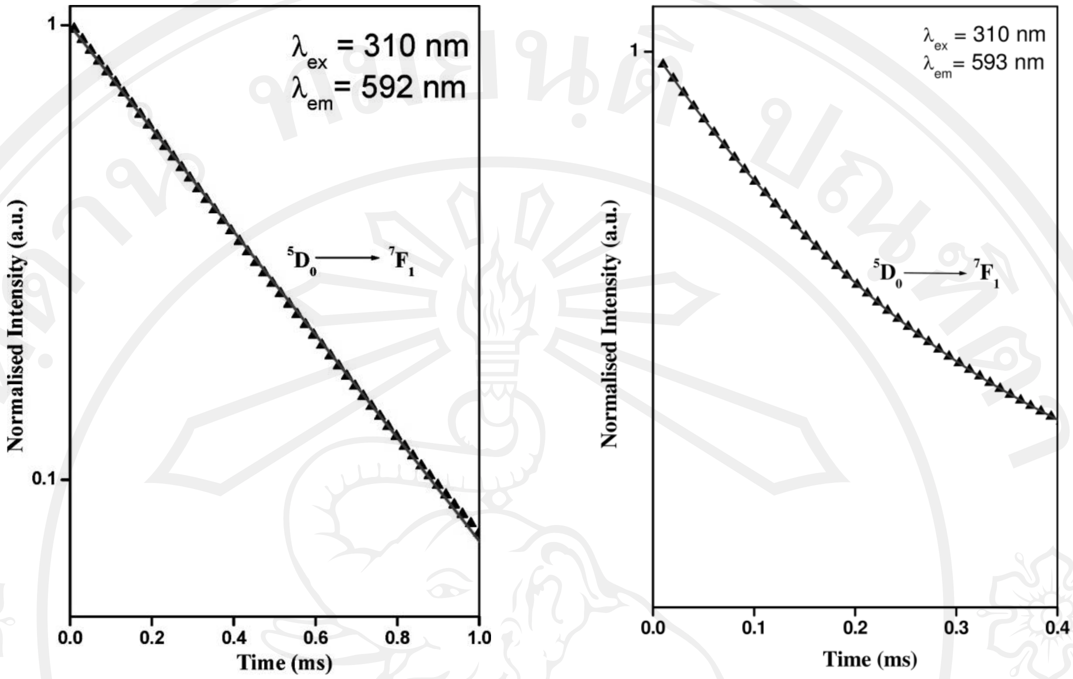

(A) (B)

Figure 4.28 Room temperature luminescence decay of the $^5D_0 \rightarrow {}^7F_1$ emission band for the 4 mol% Eu^{III} doped compound (A) **V** and (B) **VIa**.

Table 4.12 Lifetime values for the compounds **V** (4% Eu), **VIa** (4% Eu), **V** (4% Tb), and **VIa** (4% Tb).

Compound	Lifetime (in ms)
	$^5D_0 \rightarrow {}^7F_1$
V (4 mol% Eu)	0.3833
VIa (4 mol% Eu)	0.2726
	$^5D_4 \rightarrow {}^7F_6$
V (4 mol% Tb)	1.1801
VIa (4 mol% Tb)	1.3420

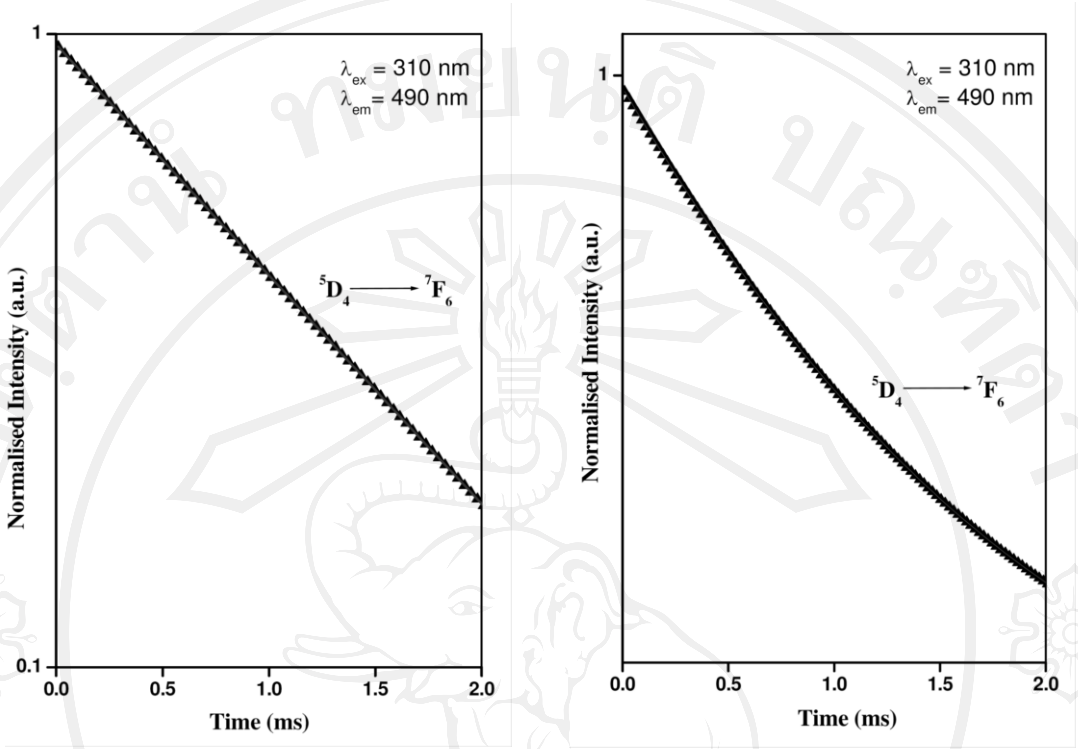

(A) (B)

Figure 4.29 Room temperature luminescence decay of the $^5D_4 \rightarrow {}^7F_6$ emission band for the 4 mol% Eu^{III} doped compound (A) **V** and (B) **VIa**.

4.2.8 Upconversion studies

There has been some recent interest in the study of a possible two–photon upconversion processes in compounds containing Nd^{III} ions [23]. The upconversion in these compounds are actually anti–Stokes emissions. Among the present compounds, $[C_{10}H_{10}N_2][Nd_2(SO_4)_4(H_2O)_2]_2$ **VIIa**, could exhibit this upconversion emission. The room temperature UV–Vis spectrum of **VIIa** indicated that the absorption increases rapidly with decreasing wavelength due to the intraligand absorption (Figure 4.30). From the UV studies, the absorption bands of the Nd^{III} ions appear to exhibit primary ground state Stark splitting of the eigenstates due to the possible crystal field effects [24].

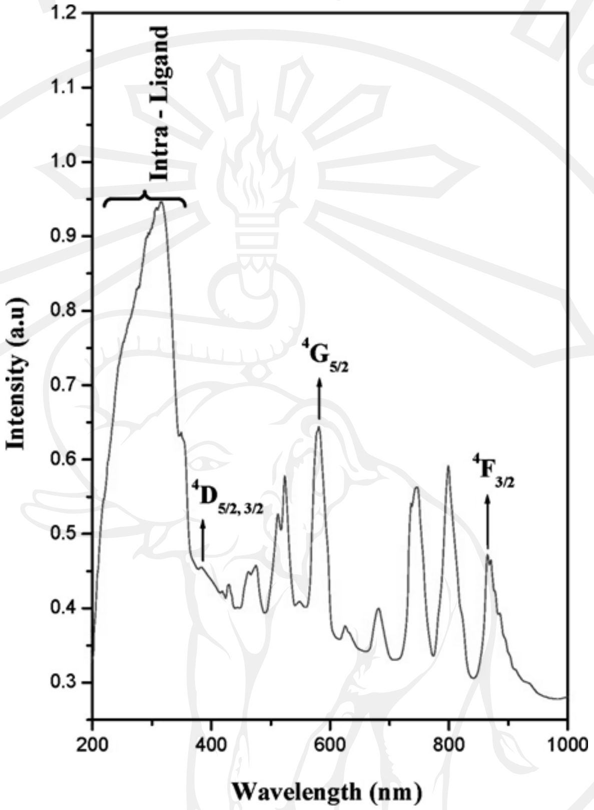

Figure 4.30 Room temperature UV−Vis spectra of compound **VIIa**.

A schematic of the energy transfer process in the upconversion using Nd^{III} ions suggests the possible pathway for the two−photon upconversion processes (Figure 4.31). The Nd^{III} compound (**VIIa**) has an intense absorption at ~582 nm, which corresponds to the $^4I_{9/2} \rightarrow {}^4G_{5/2}$ transition. This is a hypersensitive band and also satisfies the selection rules of $\Delta J = \pm 2$, $\Delta L = \pm 2$, and $\Delta S = 0$. The luminescence of **VIIa** at short wavelength results from the $^4D_{3/2}$ levels. In order to observe the possible two−photon absorption in **VIIa**, one needs to excite the photon to either the $^4D_{3/2}$ or $^4D_{5/2}$ levels. The direct excitation to this level may be limited due to the intraligand absorption by the short wavelength radiation. In addition, the excitation wavelength (λ = 582 nm) is far from the wavelength that may be required for the intraligand absorption. Thus, during our studies, the first excited $^4G_{5/2}$, level can relax nonradiatively to the $^4F_{3/2}$ level where some population can occur. This photon may further undergo excited state absorption (ESA), while the others relax to lower energy levels. The excitation wavelength (~582 nm) was used to populate the $^4F_{3/2}$ levels and efficient re–excitation from the $^4F_{3/2}$ to the $^4D_{5/2}$ levels. It is likely that the excited $^4D_{5/2}$ levels from the ESA also relax nonradiatively to the $^4D_{3/2}$ levels from which the upconverted luminescence may be observed. The upconverted luminescence spectra for this yellow pumping (582 nm excitation) from $^4D_{3/2}$ levels are shown in Figure 4.32.

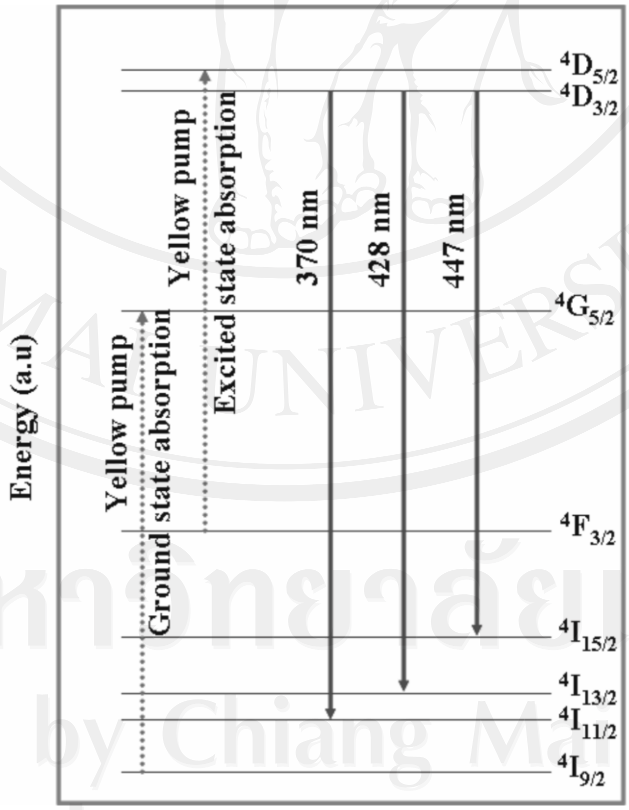

Figure 4.31 The schematic energy level diagram for Nd^{III} in compound **VIIa**.

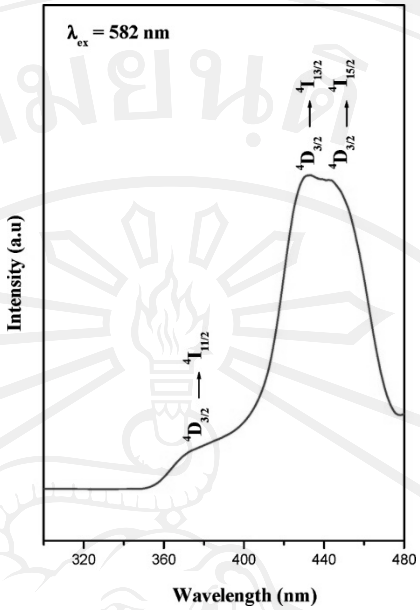

Figure 4.32 Room temperature upconversion spectra of compound **VIIa**, using 582 nm radiation.

To study the dependence of the excitation intensity on the upconverted luminescence intensity, we have also performed a simple power dependence study. Here a series of sterile glass plates are placed sequentially in the pathway between the excitation source and the sample. The decrease in excitation intensity per glass plate was precalibrated using the UV−Vis spectrometer in the transmission mode and also normalized with respect to the transmission obtained in the absence of any glass slides. The decrease in the luminescence intensity for six successive glass plates is shown in Figure 4.33. We have plotted the log–log plot of the luminescence intensity versus the excitation intensity, and a fit could provide a clue to the number of photons involved in the upconversion process (Figure 4.34). The plot for the three emission peaks at 373, 432, and 445 nm was found to be linear with a slope of 2.07, 1.57, and 1.64, respectively. These values suggest that the excitation may be due to two photons that are employed successfully. The ideal value for the two photon absorption should be closer to 2, and the decreased value may be due to the loss of some of the excitation energy at the one–photon absorption level, which could result from the $^4F_{3/2} \rightarrow {}^4I_{11/2}$, $^4F_{3/2} \rightarrow {}^4I_{9/2}$ level in the near–IR region.

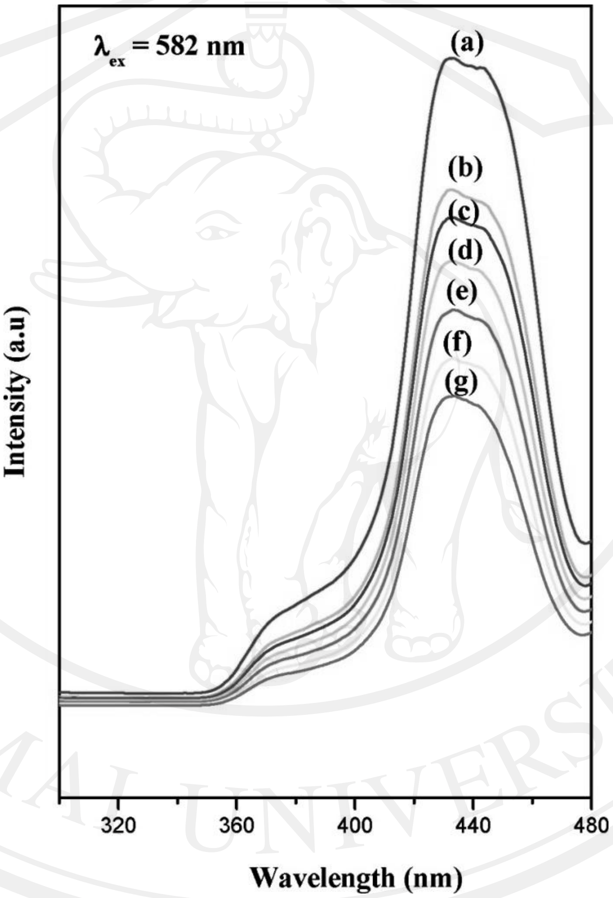

Figure 4.33 The observed emission dependence on the excitation intensity of $[Nd_2(SO_4)_4(H_2O)_2](C_{10}H_{10}N_2)$, **VIIa**. (a) 100%, (b) 90.32% (c) 85.19%, (d) 81.34%, (e) 74.86%, (f) 69.38% and (g) 63.56%.

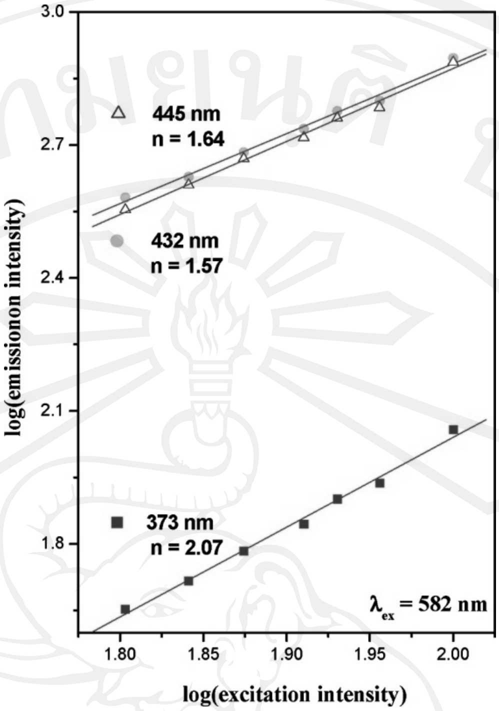

Figure 4.34 The log–log plot of the excitation intensity dependence of the luminescence intensity for *λ* = 373, 432, and 445 nm.

4.3 Conclusions

The synthesis, structure, and characterization of a family of layered lanthanide sulfate phases have been accomplished. The formation of related compounds by subtle variations of the synthesis conditions suggests the importance of the reaction parameters in the formation of framework compounds. The observation of 4,4′–bipy molecules being protonated and occupying the interlamellar spaces is important and not common. The formation of 2–D La–O–La network in **V** is noteworthy as such networks are not commonly observed. The observation of two–photon upconversion behavior in the Nd containing compound (**VIIa**) and metal centered emission in Eu^{III} (red) and Tb^{III} (green) doped samples of lanthanum (**V** and **VI**) indicates the possibility of using these compounds as optical probes.

REFERENCES

1. Y. Jiang, J. Huang, B. Kasumaj, G. Jeschke, M. Hunger, T. Mallat, A. Baiker, J. Am. Chem. Soc. 131 (2009) 2058.
2. Y. Li, L. Xie, Y. Liu, R. Yang, X. Li, Inorg. Chem. 47 (2008) 10372.
3. A. Pichon, C.M. Fierro, M. Nieuwenhuyzen, S.L. James, Cryst. Eng. Comm. 9 (2007) 449.
4. T.K. Maji, M. Ohba, S. Kitagawa, Inorg. Chem. 44 (2005) 9225.
5. K. Biradha, M. Fujita, Chem. Commun. (2001) 15.
6. S. Noro, S. Kitagawa, M. Kondo, K. Seki, Angew. Chem., Int. Ed. 39 (2000) 2082.
7. M. Kondo, T. Yoshitomi, K. Seki, H. Matsuzaka, S. Kitagawa, Angew. Chem. Int. Ed. 36 (1997) 1725.
8. A. Le Bail, H. Duroy, J.L. Fourquet, Mater. Res. Bull. 23 (1988) 447.
9. SMART (V 5.628), SAINT (V 6.45a), XPREP, SHELXTL; Bruker AXS Inc.: Madison, Wisconsin, USA, (2004).
10. G.M. Sheldrick, Siemens Area Correction Absorption Correction Program; University of Göttingen: Göttingen, Germany, (1994).
11. G.M. Sheldrick, SHELXL–97 Program for Crystal Structure Solution and Refinement; University of Göttingen: Göttingen, Germany, (1997).
12. J.L. Farrugia, WinGx suite for small–molecule single crystal crystallography, J. Appl. Crystallogr. 32 (1999) 837.
13. G.R. Desiraju, Angew. Chem. Int. Ed. Engl. 34 (1995) 2311.

14. G.R. Desiraju, Perspective in Supramolecular Chemistry: The Crystal as a Supramolecular Entity; Wiley: Chichester, (1996) 2.
15. P. Ramaswamy, N.N. Hegde, R. Prabhu, V.M. Vidya, A. Datta, S. Natarajan, Inorg. Chem. 48 (2009) 11697.
16. S. Mandal, S. Natarajan, Chem. Eur. J. 13 (2007) 968.
17. A.K. Paul, G. Madras, S. Natarajan, Dalton Trans. 39 (2010) 2263.
18. A.K. Paul, G. Madras, S. Natarajan, Cryst. Eng. Comm. 11, 2009, 55.
19. A.K. Paul, G. Madras, S. Natarajan, Phys. Chem. Chem. Phys. 11 (2009) 11285.
20. P. Mahata, K.V. Ramya, S. Natarajan, Chem. Eur. J. 14 (2008) 5839.
21. P. Mahata, K.V. Ramya, S.Natarajan, Dalton Trans. 36 (2007) 4017.
22. Z.H. Zhang, T. Okamura, Y. Hasuchika, H. Kawaguchi, L.Y. Kong, W.Y. Sun, N. Ueyam, Inorg. Chem. 44 (2005) 6219.
23. F. Auzel, Chem. Rev. 104 (2004) 139.
24. J.J. Ju, T.Y. Kwon, H.K. Kim, J.H. Kim, S.C. Kim, M.Cha, S.I. Yun, Mater. Lett. 29 (1996) 13.